Nonsmooth simulation of dense granular flows with pressure-dependent yield stress

Gilles Daviet, Florence Bertails-Descoubes

Nonsmooth simulation of dense granular flows with pressure-dependent yield stress

Gilles Daviet Florence Bertails-Descoubes *

December 1, 2015

Abstract

Understanding the flow of granular materials is of utmost importance for numerous industrial applications including the manufacturing, storing and transportation of grain assemblies (such as cement, pills, or corn), as well as for natural risk assessing considerations. Discrete Element Modeling (DEM) methods, which explicitly represent grain-grain interactions, allow for highly-tunable and precise simulations, but they suffer from a prohibitive computational cost when attempting to reproduce large scale scenarios. Continuum models have been recently investigated to overcome such scalability issues, but their numerical simulation still poses many challenges. In this work we propose a novel numerical framework for the continuous simulation of dilatable materials with pressure-dependent (Coulomb) yield stress. Relying upon convex optimization tools, we show that such a macroscopic, nonsmooth rheology can be interpreted as the exact analogous of the solid frictional contact problem at the heart of DEM methods, extended to the tensorial space. Combined with a carefully chosen finite-element discretization, this new framework allows us to avoid regularizing the continuum rheology while benefiting from the efficiency of nonsmooth optimization solvers, mainly leveraged by DEM methods so far. Our numerical results successfully compare to analytic solutions on model problems, and we retrieve qualitative flow features commonly observed in reported experiments of the literature.

1 Introduction

1.1 Motivation

Granular media are common both naturally and in industrial processes, and understanding their flow is crucial to several applications, such as studying the evolution of the pressure in a silo discharge or predicting the run-out of avalanches. Consequently, the past decades have yielded extensive bodies of research dedicated to the modeling of such materials. However, to this day their numerical simulation remains a challenging problem.

In this work we focus on a continuum model for granular-like materials satisfying two key properties. First, we assume that the material cannot be compacted, while it is allowed to dilate as desired; i.e., the divergence of the velocity field is non-negative everywhere, but not necessarily equal to zero. Second, we consider that the material behaves as a viscoplastic fluid whose yield stress depends linearly on the local pressure. Intuitively, this comes from the assumption that grain-grain interactions mostly involve rigid-body contacts with Coulomb friction.

*INRIA Grenoble Rhône-Alpes and Laboratoire Jean Kuntzman, 655 avenue de l'Europe, 38334 Saint- Ismier, France. gilles.daviet,florence.descoubes@inria.fr

1.2 Related work

1.2.1 Discrete Elements Modeling

A natural way to model granular materials is to do so at the grain level.

Stemming from the work of Jean-Jacques Moreau, nonsmooth methods for simulating frictional contacts between discrete bodies have been the subject of extensive research in the last three decades. Alart and Curnier [AC91] proposed one of the first formulation of Coulomb friction well suited for nonsmooth optimization methods. Using an operator-splitting scheme, [JAJ98, Jea99] managed to make it scale to very large number of contacts; their work became known as the *Nonsmooth Contact Dynamics* (NSCD) method. As it will be of great relevance in the following, we also point out the change of variable introduced by De Saxcé and Feng [DSF98] who reformulated the discrete-time contact problem as (nonlinear) Second-Order Cone complementarity problem. [Cad09] used this point of view to formulate a criterion for the existence of solutions, as well as an algorithm for finding one based on a series of Second-Order Cone Quadratic Programs.

Those grain-level methods are still the subject of extensive work in the context of granular materials, in regard of both their computational efficiency [AID12, KSO14] and their ability to describe specific materials [LKA14].

However, since they have to take into account every contact between grains, the cost of DEM methods increases tremendously when considering scenarios where the particles are very small w.r.t. the computational domain. This motivates the need for a continuum description of the material. Some authors have also developed hybrid methods, that try to retain the precision of DEM while tackling larger computational domains [BBS00, WW12]; in this case, an efficient way to solve the dynamics of the continuous part of the model is still required.

1.2.2 Continuous modeling of granular materials

The introduction of the $\mu(I)$ rheology [JFP06, GDR04] contributed to the growth in the last decade of a large body of research on continuous models for dry granular materials. In particular, this rheology was validated against Discrete Element Modeling simulations on complex scenarios such as the collapse of a granular column [LSP11] or the discharge of silos [SLP14].

In a very recent work, Ionescu et al. [IMBR15] were able to reproduce experimental collapses of granular columns using either the full $\mu(I)$ rheology or a constant friction coefficient μ and a constant Newtonian viscosity. Here we will focus on this latter case of a constant μ, though we show in Section 6.2.2 that our method may accommodate more complex rheologies with little modification.

Following the tradition of incompressible fluid mechanics, most works [LSP11, SLP14, IMBR15, CM14] chose to enforce a divergence-free velocity field. However, this choice may prove detrimental in certains configurations, such as the wake of an obstacle, where special care have to be taken to ensure that the rheology remains well-defined[CM14]. In contrast, our rheology will not forbid the expansion of the flow.

1.2.3 Numerical simulation of yield-stress flows

Yield-stress fluids, especially those exhibiting Bingham or Herschel–Bulkley rheologies, have been widely investigated experimentally and numerically, due to their numerous industrial applications. Most simulation methods fall into two categories:

- Regularizing methods, which employ diverse numerical artifacts to smooth out the singularities of the rheology (see [FN05] for a review). Their main benefit of regularizing strategies is their simplicity, however such methods suffer from possibly leading to very stiff equations and failing to capture properly fully rigid zones [SR01];

- Augmented Lagrangian methods, based on the framework of [FG82]. Their main drawback is the slow convergence rate often observed in practice.

Very recently, Bleyer et al. [BMdBC15] proposed a method for Herschel–Bulkley fluids based on nonsmooth convex optimization theory, which they claim benefits from much faster convergence than Augmented Lagrangian methods.

1.3 Contributions

Our contributions include

- A viscoplastic rheology with a Drucker-Prager yielding criterion and an unilateral incompressibility constraint;
- A finite-element formulation that exhibits at the discrete level a strong similarity with discrete inelastic contact mechanics;
- Algorithms for solving these equations based on the framework of [Cad09];
- A numerical validation of the overall method, including the retrieval of qualitative experimental features.

2 Notation

Let d be the dimension of the space (in practice $d = 2$ or $d = 3$). Let S_d be the space of symmetric $d \times d$ tensors. Let $\boldsymbol{\sigma} \in S_d$ and $\boldsymbol{\tau} \in S_d$, and $\boldsymbol{\sigma} : \boldsymbol{\tau} = \sum_{i,j} \boldsymbol{\sigma}_{i,j} \boldsymbol{\tau}_{i,j} \in \mathbb{R}$ be the twice-contracted product between $\boldsymbol{\sigma}$ and $\boldsymbol{\tau}$. In the following we shall use the scalar product $<\boldsymbol{\sigma}, \boldsymbol{\tau}> := \frac{\boldsymbol{\sigma}:\boldsymbol{\tau}}{2}$ on S_d and its associated norm $|\boldsymbol{\sigma}| := \sqrt{<\boldsymbol{\sigma}, \boldsymbol{\sigma}>}$.

The trace of $\boldsymbol{\sigma}$ is a scalar denoted as $\mathrm{Tr}(\boldsymbol{\sigma})$. The traceless (or deviatoric) part of $\boldsymbol{\sigma}$ is a symmetric $d \times d$ tensor defined as $\mathrm{Dev}(\boldsymbol{\sigma}) := \boldsymbol{\sigma} - \frac{1}{d}\mathbf{I}\,\mathrm{Tr}(\boldsymbol{\sigma})$, such that $\mathrm{Tr}(\mathrm{Dev}(\boldsymbol{\sigma})) = 0$.

Let $\mathbf{u}$ be the velocity field of the fluid, that is a function from $\mathbb{R}^d \times \mathbb{R}$ to $\mathbb{R}^d$ such that $\mathbf{u}(\mathbf{x}, t)$ is the macroscopic velocity of the fluid that is passing through $\mathbf{x}$ at time t. The velocity gradient of the fluid is a $d \times d$ tensor denoted $\nabla\mathbf{u}$, which contains on its j^{th} row the gradient vector of the j^{th} component of $\mathbf{u}$. The symmetric part of the velocity gradient, which will be our main variable of interest throughout the paper, is a symmetric $d \times d$ tensor defined as $\mathrm{D}(\mathbf{u}) := \frac{1}{2}(\nabla\mathbf{u} + \nabla\mathbf{u}^T)$. We have $\mathrm{Tr}(\mathrm{D}(\mathbf{u})) = \nabla\cdot\mathbf{u}$ and $\mathrm{Dev}(\mathrm{D}(\mathbf{u})) = \mathrm{D}(\mathbf{u}) - \frac{1}{d}\mathbf{I}\,\nabla\cdot\mathbf{u}$.

Finally, we introduce the symmetric tensor $\mathrm{D}^b(\mathbf{u}) := \mathrm{D}(\mathbf{u}) + \frac{b-1}{d}\mathbf{I}\nabla\cdot\mathbf{u}$, where b is a non-negative scalar. We have $\mathrm{D}^0(\mathbf{u}) = \mathrm{Dev}(\mathrm{D}(\mathbf{u}))$ and $\mathrm{D}^1(\mathbf{u}) = \mathrm{D}(\mathbf{u})$.

3 Rheology $\mathcal{DP}\,(\mu, \sigma_0)$

3.1 Definition

3.1.1 Pressure-dependent yield-stress fluid

We consider a rheology combining a constant Newtonian viscosity η with a yield-stress $\kappa_{\mu,\boldsymbol{\sigma}_0}(p)$ that linearly depends on the pressure p,

$$\kappa_{\mu,\boldsymbol{\sigma}_0}(p) = \boldsymbol{\sigma}_0 + \mu p,$$

similarly as in [IMBR15].

The total stress tensor $\boldsymbol{\sigma}_{tot}$ is defined as[1]

$$\boldsymbol{\sigma}_{tot} := 2\eta\,\mathrm{D}^b(\mathbf{u}) + \boldsymbol{\tau} - p\mathbf{I},$$

[1] Using the more general $\mathrm{D}^b(\mathbf{u})$ rather than the usual $\mathrm{D}^0(\mathbf{u})$ for the Newtonian viscosity allows us to model a possibly non-zero bulk viscosity.

where $\boldsymbol{\tau}$ is a traceless symmetric tensor satisfying

$$\begin{cases} \boldsymbol{\tau} = \kappa_{\mu,\boldsymbol{\sigma}_0}\left(\sqrt{\frac{d}{2}}\,p\right)\dfrac{\mathrm{D}^0(\mathbf{u})}{|\,\mathrm{D}^0(\mathbf{u})|} & \text{if } \mathrm{D}^0(\mathbf{u}) \neq \mathbf{0} \quad (1a) \\ |\boldsymbol{\tau}| \leq \kappa_{\mu,\boldsymbol{\sigma}_0}\left(\sqrt{\frac{d}{2}}\,p\right) & \text{if } \mathrm{D}^0(\mathbf{u}) = \mathbf{0}, \quad (1b) \end{cases}$$

We chose to incorporate the factor $\sqrt{\frac{d}{2}}$ in the above definition in order to lighten the notations in the following sections. Note that in the 2D case, μ coincides with the usual Mohr-Coulomb definition of the friction coefficient: $\mu := \sin\varphi$, with φ the angle of friction.

Remark 1. *We used $|\boldsymbol{\tau}|$ in (1b) instead of the usual $|\,\mathrm{Dev}(\boldsymbol{\sigma}_{tot})|$. But since $\mathrm{Dev}(\boldsymbol{\sigma}_{tot}) = 2\eta b\,\mathrm{D}^0(\mathbf{u}) + \boldsymbol{\tau}$, in the non-flowing case (1b) where $\mathrm{D}^0(\mathbf{u}) = 0$, we have $|\,\mathrm{Dev}(\boldsymbol{\sigma}_{tot})| = |\boldsymbol{\tau}|$.*

3.1.2 Dilatability

Most continuum-based models for granulars consider the fluid to be perfectly incompressible. In contrast, we take into account the typically asymmetric yielding behavior of granulars by allowing the fluid to expand as much as desired, while strictly preventing compaction. To capture this unilateral phenomenon, the pressure p is set to enforce the non-compaction unilateral constraint $\nabla\cdot\mathbf{u} \geq 0$. This can be formulated as

$$\begin{cases} p \geq 0 & \text{if } \nabla\cdot\mathbf{u} = 0 \\ p = 0 & \text{if } \nabla\cdot\mathbf{u} > 0 \end{cases}$$

or, using an equivalent complementarity notation,

$$0 \leq p \perp \nabla\cdot\mathbf{u} \geq 0, \quad (2)$$

where the notation $\alpha \perp \beta$ with $\alpha \in \mathbb{R}$ and $\beta \in \mathbb{R}$ means that at least one of the two scalars should vanish. If they are furthermore requested to be nonnegative, which is our case here, it means that α and β cannot both be strictly positive at the same time.

In our results section, we shall see that relaxing the common incompressibility assumption $\nabla\cdot\mathbf{u} = 0$ prevents the arising of an ill-defined rheology in some typical scenarios such as the flow in the wake of an obstacle [CM14]. Moreover our complementarity constraint (2) naturally fits in with our numerical framework, without adding any computational cumbersomeness.

3.1.3 Cases covered by our choice of rheology

Much like in [IMBR15], our set of parameters allows us to explore an interesting range of constitutive laws. When $\mu = 0$, we retrieve the viscoplastic Bingham rheology, while when taking $\eta = 0$ and $\sigma_0 = 0$, we get a purely Coulomb plastic flow — or, in other terms, the $\mu(I)$ rheology with a constant inertial number I.

The numerical method for the quasistatic simulation presented in Section 4 will require a non-zero η to obtain a well-posed system. However, this constraint will be alleviated in Section 5 when using temporal schemes. In our numerical experiments, we were also able to simulate the complete $\mu(I)$ rheology by explicitly computing the inertial number I at each time step.

Note also that the σ_0 coefficient should not be assimilated to the usual *cohesion* term. Indeed, in our case the additional stress due to this coefficient will always be tangential, and may be non-zero when $\nabla\cdot\mathbf{u} > 0$. In this regard, σ_0 should rather be used to model effects related to the geometry of grains. If we were to model proper cohesion c, we could do so by defining $\kappa(p) := \mu(p+c)$, and the pressure unilateral constraint as $0 \leq p+c \perp \nabla\cdot\mathbf{u} \geq 0$. However

in the framework presented below, thanks to a change of variable this would be stricly equivalent to adding a positive confining pressure to the right-hand side of the conservation of momentum equation. In the following, we shall thus free ourselves from modeling such a cohesion effect explicitly.

3.1.4 Solution set $\mathcal{DP}(\mu, \sigma_0)$

Let us introduce the symmetric tensor $\boldsymbol{\lambda} := 2\eta\, \mathrm{D}^b(\mathbf{u}) - \boldsymbol{\sigma}_{tot} = p\mathbf{I} - \boldsymbol{\tau}$. Using the identities $p = \frac{1}{d}\operatorname{Tr}(\boldsymbol{\lambda})$ and $\boldsymbol{\tau} = -\operatorname{Dev}\boldsymbol{\lambda}$, and the definition of $\mathrm{D}(\mathbf{u})$, our Drucker-Prager rheology (1 — 2) can be directly rewritten as

$$\begin{cases} \operatorname{Dev}(\boldsymbol{\lambda}) = -\kappa_{\mu,\boldsymbol{\sigma}_0}\left(\dfrac{\operatorname{Tr}(\boldsymbol{\lambda})}{\sqrt{2d}}\right)\dfrac{\operatorname{Dev}(\mathrm{D}(\mathbf{u}))}{|\operatorname{Dev}(\mathrm{D}(\mathbf{u}))|} & \text{if } \operatorname{Dev}(\mathrm{D}(\mathbf{u})) \neq \mathbf{0} \quad (3a) \\ |\operatorname{Dev}(\boldsymbol{\lambda})| \leq \kappa_{\mu,\boldsymbol{\sigma}_0}\left(\dfrac{\operatorname{Tr}(\boldsymbol{\lambda})}{\sqrt{2d}}\right) & \text{if } \operatorname{Dev}(\mathrm{D}(\mathbf{u})) = \mathbf{0}, \quad (3b) \\ 0 \leq \dfrac{1}{d}\operatorname{Tr}(\boldsymbol{\lambda}) \perp \operatorname{Tr}(\mathrm{D}(\mathbf{u})) \geq 0. & (3c) \end{cases}$$

In the remainder of this paper, we shall denote by $\mathcal{DP}(\mu, \sigma_0) \subset S_d^2$ the set of tensors $(\boldsymbol{\lambda}; \mathrm{D}(\mathbf{u})) \in S_d \times S_d$ satisfying (3).

3.2 Analogy with solid frictional contact

3.2.1 Solid Signorini-Coulomb law

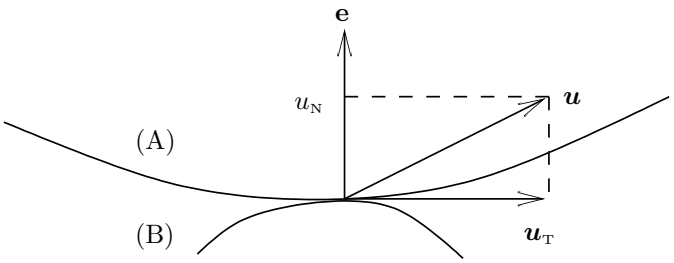

Figure 1: Local contact basis, with normal and tangent subspaces.

We briefly recall the Signorini-Coulomb friction law in the case of two solid objects (A) and (B) with a single contact point, as illustrated in Figure 1. Let $\boldsymbol{u} \in \mathbb{R}^d$ be the relative velocity between the two colliding objects, $\boldsymbol{u} := \boldsymbol{u}_A - \boldsymbol{u}_B$, and $\boldsymbol{r} \in \mathbb{R}^d$ be the reaction force applied by object (B) onto object (A). We suppose that the surface of contact is sufficiently smooth so that the normal $\mathbf{e} \in \mathbb{R}^d$ at the contact point can be uniquely defined.

Disjunctive formulation The Signorini-Coulomb law for contact with dry friction states that the couple $(\boldsymbol{r}, \boldsymbol{u})$ has to satisfy at least one of the following cases,

$$\begin{cases} \boldsymbol{r} = 0 \text{ and } u_N \geq 0 & \text{Take-off case} \\ \|\boldsymbol{r}_T\| \leq \mu\, r_N \text{ and } \boldsymbol{u} = 0 & \text{Sticking case} \\ \|\boldsymbol{r}_T\| = \mu\, r_N, u_N = 0 \text{ and } \exists \alpha > 0, \boldsymbol{u}_T = -\alpha \boldsymbol{r}_T & \text{Sliding case,} \end{cases} \quad (4)$$

where $x_N \in \mathbb{R}$ and $\boldsymbol{x}_T \in \mathbb{R}^{d-1}$ are the normal and tangential components of vector $\boldsymbol{x} \in \mathbb{R}^d$, respectively, μ is the coefficient of friction at contact point, and $\|\cdot\|$ is the Euclidean norm on $\mathbb{R}^d$. Let denote by $\mathcal{C}(\mu) \subset \mathbb{R}^d \times \mathbb{R}^d$ the set of $(\boldsymbol{r}, \boldsymbol{u})$ satisfying (4).

Functional formulations Though classical, the disjunctive formulation (4) is not always the most convenient to work with in a numerical setup. Typically, one may prefer to express the Signorini-Coulomb law as a root-finding problem, i.e., in the form

$$(\boldsymbol{r},\boldsymbol{u}) \in \mathcal{C}(\mu) \iff f(\boldsymbol{r},\boldsymbol{u}) = 0, \tag{5}$$

where f is a nonsmooth function from $\mathbb{R}^d \times \mathbb{R}^d$ to $\mathbb{R}^d$.

One classical example of such a nonsmooth function was notably provided by Alart and Curnier [AC91], and defined as

$$\begin{array}{rccc} f_{\mathrm{AC}} & : & \mathbb{R}^d \times \mathbb{R}^d & \longrightarrow & \mathbb{R}^d \\ & & (\boldsymbol{r},\boldsymbol{u}) & \longmapsto & \left(\begin{array}{l} \Pi_{\mathbb{R}_+}\left(r_{\mathrm{N}} - \xi_{\mathrm{N}} u_{\mathrm{N}}\right) - r_{\mathrm{N}} \\ \Pi_{\mathcal{B}^{d-1}(\mu r_{\mathrm{N}})}\left(\boldsymbol{r}_{\mathrm{T}} - \xi_{\mathrm{T}} \boldsymbol{u}_{\mathrm{T}}\right) - \boldsymbol{r}_{\mathrm{T}} \end{array} \right), \end{array}$$

where $\Pi_{\mathcal{C}}$ is the orthogonal projection operator on the convex space $\mathcal{C}$, ξ_{T} and ξ_{N} are positive real numbers, and $\mathcal{B}^{d-1}(a) \subset \mathbb{R}^{d-1}$ is the ball of radius $a \geq 0$ centered at the origin.

Another well-known function satisfying (5) may be derived based upon De Saxcé and Feng [DSF98]'s work. Indeed, thanks to their proposed change of variable, $\hat{\boldsymbol{u}} = \boldsymbol{u} + \mu \|\boldsymbol{u}_{\mathrm{T}}\| \mathbf{e}$, the Coulomb law may be written compactly as

$$\mathcal{K}^d_{\frac{1}{\mu}} \ni \hat{\boldsymbol{u}} \perp \boldsymbol{r} \in \mathcal{K}^d_{\mu}, \tag{6}$$

where the complementarity notation refers to the standard orthogonality in $\mathbb{R}^d$, and where $\mathcal{K}^d_{\mu} \subset \mathbb{R}^d$ is the second-order cone (**SOC**) of aperture μ (see Figure 2, left), generally defined on $\mathbb{R}^n$ $(n \geq 2)$ as

$$\mathcal{K}^n_{\mu} := \left\{ (x_{\mathrm{N}}, \boldsymbol{x}_{\mathrm{T}}) \in \mathbb{R} \times \mathbb{R}^{n-1}, \|\boldsymbol{x}_{\mathrm{T}}\| \leq \mu x_{\mathrm{N}} \right\}. \tag{7}$$

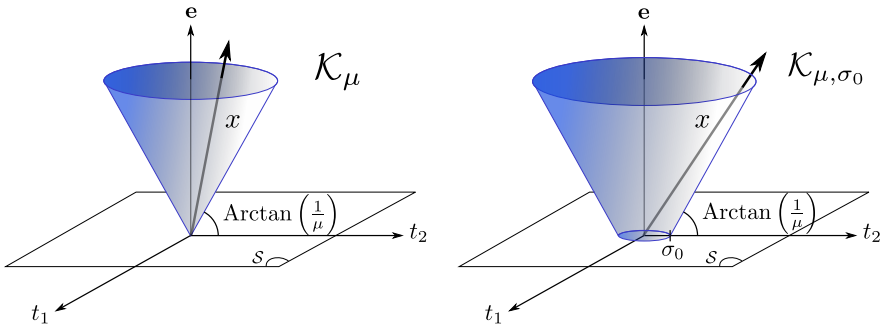

Figure 2: The second-order cone (left) and the truncated second-order cone (right) represented in 3D ($n = 3$).

Now, let us recall the definition of the normal cone to a convex set $\mathcal{C} \subset \mathbb{R}^n$ at point $\boldsymbol{x} \in \mathbb{R}^n$,

$$\begin{array}{ll} \mathcal{N}_{\mathcal{C}}(\boldsymbol{x}) := \left\{ \boldsymbol{y} \in \mathbb{R}^n,\ \boldsymbol{y}^{\top}(\boldsymbol{z} - \boldsymbol{x}) \leq 0\ \forall \boldsymbol{z} \in \mathcal{C} \right\} & \text{if } \boldsymbol{x} \in \mathcal{C} \\ \mathcal{N}_{\mathcal{C}}(\boldsymbol{x}) := \varnothing & \text{if } \boldsymbol{x} \in \mathbb{R}^n - \mathcal{C}. \end{array} \tag{8}$$

Note that for an interior point $\boldsymbol{x} \in \operatorname{Int}\mathcal{C}$, we have $\mathcal{N}_C(x) = \{0\}$. Moreover, in the particular case when C has a smooth boundary, then on each point $\boldsymbol{x}$ of the boundary $\operatorname{Bd}\mathcal{C}$, the normal cone is spanned by the outward normal $\mathbf{n}_{\mathcal{C}}(\boldsymbol{x})$ to $\mathcal{C}$ at $\boldsymbol{x}$, i.e., $\mathcal{N}_{\mathcal{C}}(\boldsymbol{x} \in \operatorname{Bd}\mathcal{C}) = \{\alpha\, \mathbf{n}_{\mathcal{C}}(\boldsymbol{x}), \alpha \in \mathbb{R}_+\}$.

Let ξ be a positive scalar, $\boldsymbol{x} \in \mathbb{R}^n$ and $\boldsymbol{y} \in \mathbb{R}^n$. From the projection theorem (see, e.g., [HUL01, Proposition A.5.3.3]), we have

$$\Pi_{\mathcal{C}}(\boldsymbol{x} - \xi \boldsymbol{y}) = \boldsymbol{x} \iff \boldsymbol{y} \in -\mathcal{N}_{\mathcal{C}}(\boldsymbol{x}). \tag{9}$$

In the particular case where $C = \mathcal{K}_\mu^n$, we have moreover

$$\boldsymbol{y} \in -\mathcal{N}_C(\boldsymbol{x}) \iff \mathcal{K}_{\frac{1}{\mu}}^n \ni \boldsymbol{y} \perp \boldsymbol{x} \in \mathcal{K}_\mu^n. \tag{10}$$

Based on (6), (9) and (10), one may then derive the so-called De Saxcé function satisfying (5),

$$\begin{array}{rccc} f_{\mathrm{DS}} & : & \mathbb{R}^d \times \mathbb{R}^d & \longrightarrow & \mathbb{R}^d \\ & & (\boldsymbol{r}, \boldsymbol{u}) & \longmapsto & \Pi_{\mathcal{K}_\mu^d}(\boldsymbol{r} - \xi\hat{\boldsymbol{u}}) - \boldsymbol{r}, \end{array}$$

where ξ is a positive real number.

In Section 3.2.3 we will show that extended versions of both the Alart-Curnier and De Saxcé functions will play a similar role for our continuum granular rheology $\mathcal{DP}(\mu, \sigma_0)$. But since the above contact problem only involves the canonical Euclidean space $\mathbb{R}^d$, we first need to introduce some mathematical tools in order to transpose it to the space of symmetric tensors.

3.2.2 Preliminary tools

Recall that S_d is the space of $d \times d$ symmetric tensors. Let $\mathfrak{s}(d) := \dim S_d = \frac{d(d+1)}{2}$. The dimension of the hyperplane of traceless tensors in S_d is $\mathfrak{t}(d) := \mathfrak{s}(d) - 1 = (d-1)(1+\frac{d}{2})$.

Definition 1. *Let us introduce the morphism χ,*

$$\begin{array}{rcll} \chi : \mathbb{R} \times \mathbb{R}^{\mathfrak{t}(d)} & \to & S_d & \\ (a; b, c) & \mapsto & \begin{pmatrix} a+b & c \\ c & a-b \end{pmatrix} & \text{if } d = 2 \\ (a; b, c, d, e, f) & \mapsto & \begin{pmatrix} \frac{\sqrt{2}}{\sqrt{3}}a + b - \frac{c}{\sqrt{3}} & d & e \\ d & \frac{\sqrt{2}}{\sqrt{3}}a - b - \frac{c}{\sqrt{3}} & f \\ e & f & \frac{\sqrt{2}}{\sqrt{3}}a + \frac{2c}{\sqrt{3}} \end{pmatrix} & \text{if } d = 3. \end{array}$$

Property 1. *χ is an orthonormal isomorphism between the two Euclidean spaces $\left(\mathbb{R}^{\mathfrak{s}(d)}; \cdot^\top \cdot\right)$ and $(S_d; <\cdot, \cdot>)$. This means*

$$\forall (\boldsymbol{x}, \boldsymbol{y}) \in \mathbb{R}^{\mathfrak{s}(d)} \times \mathbb{R}^{\mathfrak{s}(d)} \ \boldsymbol{x}^\top \boldsymbol{y} = <\chi(\boldsymbol{x}), \chi(\boldsymbol{y})>, \tag{11}$$

where $\boldsymbol{x}^\top \boldsymbol{y}$ is the usual scalar product on $\mathbb{R}^m, m \geq 1$ and $<\boldsymbol{\sigma}, \boldsymbol{\tau}> = \frac{\boldsymbol{\sigma} : \boldsymbol{\tau}}{2}$ is our scalar product on S_d.

Proof. Let $\|\boldsymbol{x}\| = \sqrt{\boldsymbol{x}^\top \boldsymbol{x}}$ be the Euclidean norm of $\boldsymbol{x} \in \mathbb{R}^m, m \geq 1$. Direct calculations show that

$$\begin{array}{rl} |\chi(a; b, c)|^2 = a^2 + b^2 + c^2 = \|(a; b, c)\|^2 & \text{when } d = 2 \\ |\chi(a; b, c, d, e, f)|^2 = a^2 + b^2 + c^2 + d^2 + e^2 + f^2 = \|(a; b, c, d, e, f)\|^2 & \text{when } d = 3, \end{array}$$

meaning that

$$\forall \boldsymbol{x} \in \mathbb{R}^{\mathfrak{s}(d)} \ \|\boldsymbol{x}\| = |\chi(\boldsymbol{x})|. \tag{12}$$

By decomposing the scalar product, we get

$$\begin{aligned} \forall (\boldsymbol{x}, \boldsymbol{y}) \in \mathbb{R}^{\mathfrak{s}(d)} \times \mathbb{R}^{\mathfrak{s}(d)}, \ \boldsymbol{x}^\top \boldsymbol{y} &= \frac{1}{2}\left(\|\boldsymbol{x} + \boldsymbol{y}\|^2 - \|\boldsymbol{x}\|^2 - \|\boldsymbol{y}\|^2\right) \\ &= \frac{1}{2}\left(|\chi(\boldsymbol{x} + \boldsymbol{y})|^2 - |\chi(\boldsymbol{x})|^2 - |\chi(\boldsymbol{y})|^2\right) \text{ from (12)} \\ &= <\chi(\boldsymbol{x}), \chi(\boldsymbol{y})> \quad \text{using the linearity of } \chi. \end{aligned}$$

□

Property 2. *Let us use the notation* $(\sigma_N;\boldsymbol{\sigma}_T) \coloneqq \overline{\boldsymbol{\sigma}} \coloneqq \chi^{-1}(\boldsymbol{\sigma})$ *to decompose a symmetric tensor* $\boldsymbol{\sigma} \in S_d$ *or its preimage by* χ, $\overline{\boldsymbol{\sigma}} \in \mathbb{R}^{\mathfrak{s}(d)}$, *into a* normal component $\sigma_N \in \mathbb{R}$ *and a* tangential *component* $\boldsymbol{\sigma}_T \in \mathbb{R}^{\mathfrak{t}(d)}$. *We have*

$$\frac{1}{\sqrt{2d}}\operatorname{Tr}(\boldsymbol{\sigma}) = \sigma_N \tag{13a}$$

$$\textit{and} \quad |\operatorname{Dev}(\boldsymbol{\sigma})| = \|\boldsymbol{\sigma}_T\|. \tag{13b}$$

Proof. By linearity of χ, we have $\boldsymbol{\sigma} = \chi(\sigma_N;\boldsymbol{\sigma}_T) = \chi(\sigma_N;0) + \chi(0;\boldsymbol{\sigma}_T)$. Then, by linearity of the trace and by noting from the definition of χ that $\operatorname{Tr}(\chi(0;\boldsymbol{\sigma}_T)) = 0$, it follows that $\operatorname{Tr}(\boldsymbol{\sigma}) = \operatorname{Tr}(\chi(\sigma_N;0)) = \sqrt{2d}\,\sigma_N$.

Likewise, by linearity of the Dev operator and by noting from the definition of χ that $\operatorname{Dev}(\chi(\sigma_N;0)) = 0$, we have

$$\begin{aligned}\operatorname{Dev}(\boldsymbol{\sigma}) &= \operatorname{Dev}(\chi(0;\boldsymbol{\sigma}_T)) \\ &= \chi(0;\boldsymbol{\sigma}_T) - \frac{1}{d}\mathbf{I}\underbrace{\operatorname{Tr}(\chi(0;\boldsymbol{\sigma}_T))}_{=0}\end{aligned}$$

and therefore from (12) we get $|\operatorname{Dev}(\boldsymbol{\sigma})| = \|(0;\boldsymbol{\sigma}_T)\| = \|\boldsymbol{\sigma}_T\|$.

□

3.2.3 Reformulation of our rheology $\mathcal{DP}(\mu,\sigma_0)$ on $\mathbb{R}^{\mathfrak{s}(d)}$

Thanks to our isomorphism χ, our Drucker-Prager rheology $\mathcal{DP}(\mu,\sigma_0)$ (see Section 3.1.4), initially expressed on the tensorial space S_d, can be reformulated on $R^{\mathfrak{s}(d)}$.

Theorem 1. *Using the notations of Property 2, the rheology* $\mathcal{DP}(\mu,\sigma_0)$ *can be equivalently expressed as*

$$\begin{cases} \boldsymbol{\lambda}_T = -\kappa_{\mu,\boldsymbol{\sigma}_0}(\lambda_N)\dfrac{\mathrm{D}(\mathbf{u})_T}{\|\mathrm{D}(\mathbf{u})_T\|} & \textit{if } \mathrm{D}(\mathbf{u})_T \neq \mathbf{0} \quad (14a)\\ \|\boldsymbol{\lambda}_T\| \le \kappa_{\mu,\boldsymbol{\sigma}_0}(\lambda_N) & \textit{if } \mathrm{D}(\mathbf{u})_T = \mathbf{0}, \quad (14b)\\ 0 \le \lambda_N \perp \mathrm{D}(\mathbf{u})_N \ge 0, & (14c)\end{cases}$$

that is,

$$(\boldsymbol{\lambda};\mathrm{D}(\mathbf{u})) \in \mathcal{DP}(\mu,\sigma_0) \iff \left(\overline{\boldsymbol{\lambda}};\overline{\mathrm{D}(\mathbf{u})}\right) \textit{ satisfies Problem (14).} \tag{15}$$

Proof. Using (13a) we get $\operatorname{Tr}\boldsymbol{\lambda} = \sqrt{2d}\,\lambda_N$. Since $|\operatorname{Dev}(\mathrm{D}(\mathbf{u}))| = \|\mathrm{D}(\mathbf{u})_T\|$ from (13b), we have $\operatorname{Dev}(\mathrm{D}(\mathbf{u})) = \mathbf{0} \iff \mathrm{D}(\mathbf{u})_T = \mathbf{0}$. Thus, it is straightforward to see that the scalar equation (3b) is equivalent to (14b).

Moreover,

$$(3a) \iff \left(\mathrm{D}(\mathbf{u})_T \neq \mathbf{0} \implies \begin{cases} |\operatorname{Dev}(\boldsymbol{\lambda})| = \kappa_{\mu,\boldsymbol{\sigma}_0}(\lambda_N) \\ -\operatorname{Dev}(\boldsymbol{\lambda}) \text{ collinear to } \operatorname{Dev}(\mathrm{D}(\mathbf{u})) \end{cases}\right).$$

Since χ is orthonormal, it preserves both norm and collinearity. Therefore,

$$\begin{aligned}(3a) &\iff \left(\mathrm{D}(\mathbf{u})_T \neq \mathbf{0} \implies \begin{cases} \|\boldsymbol{\lambda}_T\| = \kappa_{\mu,\boldsymbol{\sigma}_0}(\lambda_N) \\ -\boldsymbol{\lambda}_T \text{ collinear to } \mathrm{D}(\mathbf{u})_T \end{cases}\right) \\ &\iff (14a).\end{aligned}$$

Finally, from Property (13a) the scalar complementarity (3c) rereads

$$0 \le \sqrt{2d}\,\mathrm{D}(\mathbf{u})_N \perp \sqrt{\frac{2}{d}}\,\lambda_N \ge 0,$$

which is equivalent to (14c) since complementarity is insensitive to strictly positive scaling factors. □

Problem (14), which now depends on vector variables, looks very similar to the disjunctive formulation (4) of the Coulomb friction law $\mathcal{C}(\mu)$ between discrete bodies, where $\overline{\boldsymbol{\lambda}}$ plays the role[2] of the reaction force $\boldsymbol{r}$, and $\overline{\mathrm{D}(\mathbf{u})}$ that of the relative velocity $\boldsymbol{u}$. Actually we shall see in the following section that in the special case where our fluid rheology is considered to be bidimensional ($d = 2$) and where $\sigma_0 = 0$, Problem (14) then becomes exactly equivalent to the tridimensional discrete law $\mathcal{C}(\mu)$.

3.2.4 Functional formulations of our rheology $\mathcal{DP}(\mu, \sigma_0)$ on $\mathbb{R}^{\mathfrak{s}(d)}$

In this section, we show that similar functional formulations as those introduced in Section 3.2.1 for the solid contact law $\mathcal{C}(\mu)$ do apply to our fluid rheology $\mathcal{DP}(\mu, \sigma_0)$.

Extended Alart-Curnier formulation

Definition 2. *Let us introduce the following extension of the Alart-Curnier function,*

$$
\begin{array}{rccc}
f_{AC}^{\star} & : & \mathbb{R}^{\mathfrak{s}(d)} \times \mathbb{R}^{\mathfrak{s}(d)} & \longrightarrow & \mathbb{R}^{\mathfrak{s}(d)} \\
 & & (\overline{\boldsymbol{\lambda}}, \overline{\mathrm{D}(\mathbf{u})}) & \longmapsto & \begin{pmatrix} \Pi_{\mathbb{R}_+}\left(\lambda_N - \xi_N \mathrm{D}(\mathbf{u})_N\right) - \lambda_N \\ \Pi_{\mathcal{B}^{\mathfrak{t}(d)}(\kappa_{\mu,\boldsymbol{\sigma}_0}(\lambda_N))}\left(\boldsymbol{\lambda}_T - \xi_T \mathrm{D}(\mathbf{u})_T\right) - \boldsymbol{\lambda}_T \end{pmatrix}
\end{array}
$$

where ξ_T and ξ_N are positive real numbers, and $\mathcal{B}^{\mathfrak{t}(d)}(a) \subset \mathbb{R}^{\mathfrak{t}(d)}$ is the ball of radius $a \geq 0$ centered at the origin.

Theorem 2. *The following equivalence holds,*

$$
(\boldsymbol{\lambda}; \mathrm{D}(\mathbf{u})) \in \mathcal{DP}(\mu, \sigma_0) \iff f_{AC}^{\star}(\overline{\boldsymbol{\lambda}}, \overline{\mathrm{D}(\mathbf{u})}) = 0. \tag{16}
$$

Proof. Given Theorem(1), it is enough to show that $f_{\mathrm{AC}}^{\star}(\overline{\boldsymbol{\lambda}}, \overline{\mathrm{D}(\mathbf{u})}) = 0$ if and only if $\left(\overline{\boldsymbol{\lambda}}; \overline{\mathrm{D}(\mathbf{u})}\right)$ satisfies Problem (14). Let us first introduce two lemmas for reinterpreting (14).

Lemma 1. *The complementarity condition (14c) can be written in a disjunctive fashion as*

$$
(14c) \iff \begin{cases} \lambda_N \geq 0 & \\ \mathrm{D}(\mathbf{u})_N \geq 0 & \text{if } \lambda_N = 0 \\ \mathrm{D}(\mathbf{u})_N = 0 & \text{if } \lambda_N > 0. \end{cases}
$$

Lemma 2. *If $\kappa_{\mu,\boldsymbol{\sigma}_0}(\lambda_N) > 0$, Conditions (14a — 14b) reread*

$$
(14a - 14b) \iff \begin{cases} \|\boldsymbol{\lambda}_T\| \leq \kappa_{\mu,\boldsymbol{\sigma}_0}(\lambda_N) & \\ \mathrm{D}(\mathbf{u})_T = -\alpha \boldsymbol{\lambda}_T,\ \alpha \in \mathbb{R}_+ & \text{if } \|\boldsymbol{\lambda}_T\| = \kappa_{\mu,\boldsymbol{\sigma}_0}(\lambda_N) \\ \mathrm{D}(\mathbf{u})_T = 0 & \text{if } \|\boldsymbol{\lambda}_T\| < \kappa_{\mu,\boldsymbol{\sigma}_0}(\lambda_N). \end{cases}
$$

Let us now have a look at the normal part of $f_{\mathrm{AC}}^{\star}$, where $\mathcal{C} = \mathbb{R}_+$. Using the normal cone defined in (8), we have $\mathcal{N}_{\mathcal{C}}(0) = \mathbb{R}^-$ and $\mathcal{N}_{\mathcal{C}}(x > 0) = \{0\}$. Therefore, according to (9) we get

$$
\begin{aligned}
x = \Pi_{\mathcal{C}}(x - \xi y) &\iff y \in -\mathcal{N}_{\mathcal{C}}(x) \\
&\iff \begin{cases} x \in \mathcal{C} & \\ y \in \mathbb{R}_+ & \text{if } x = 0 \\ y = 0 & \text{if } x > 0. \end{cases}
\end{aligned}
$$

For $x = \lambda_{\mathrm{N}}$, $y = \mathrm{D}(\mathbf{u})_{\mathrm{N}}$, and $\xi = \xi_{\mathrm{N}}$, we thus identify using Lemma 1 that

$$
f_{\mathrm{AC}}^{\star}(\overline{\boldsymbol{\lambda}}, \overline{\mathrm{D}(\mathbf{u})})_{\mathrm{N}} = 0 \iff (14c),
$$

[2]Note however that the tangential counterparts of $\overline{\boldsymbol{\lambda}}$ and $\boldsymbol{r}$, and of $\overline{\mathrm{D}(\mathbf{u})}$ and $\boldsymbol{u}$ respectively, do not share the same dimension. For instance, when $d = 3$, $\boldsymbol{\lambda}_{\mathrm{T}} \in \mathbb{R}^5$ and $\mathrm{D}(\mathbf{u})_{\mathrm{T}} \in \mathbb{R}^5$ while $\boldsymbol{r}_{\mathrm{T}} \in \mathbb{R}^2$ and $\boldsymbol{u}_{\mathrm{T}} \in \mathbb{R}^2$.

where $f^\star_{\mathrm{AC}}(\overline{\boldsymbol{\lambda}}, \overline{\mathrm{D}(\mathbf{u})})_{\mathrm{N}}$ denotes the first component (normal part) of $f^\star_{\mathrm{AC}}(\overline{\boldsymbol{\lambda}}, \overline{\mathrm{D}(\mathbf{u})})$.

Let us now consider the tangential part of $f^\star_{\mathrm{AC}}$, where $\mathcal{C} = \mathcal{B}^{\mathfrak{t}(d)}(\kappa_{\mu,\boldsymbol{\sigma}_0}(\lambda_{\mathrm{N}}))$. Let us first assume that $\kappa_{\mu,\boldsymbol{\sigma}_0}(\lambda_{\mathrm{N}}) > 0$. We then have $\mathcal{N}_{\mathcal{C}}(\boldsymbol{x} \in \operatorname{Int}\mathcal{C}) = \{\mathbf{0}\}$ and $\mathcal{N}_{\mathcal{C}}(\boldsymbol{x} \in \operatorname{Bd}\mathcal{C}) = \left\{\alpha \frac{\boldsymbol{x}}{\|\boldsymbol{x}\|}, \alpha \in \mathbb{R}_+\right\}$, where $\operatorname{Int}\mathcal{C}$ is the interior of $\mathcal{C}$ and $\operatorname{Bd}\mathcal{C}$ its boundary. Using (9), we get

$$\begin{aligned}
\boldsymbol{x} = \Pi_{\mathcal{C}}(\boldsymbol{x} - \xi\boldsymbol{y}) &\iff \boldsymbol{y} \in -\mathcal{N}_{\mathcal{C}}(\boldsymbol{x}) \\
&\iff \begin{cases} \boldsymbol{x} \in \mathcal{C} & \\ \boldsymbol{y} = \mathbf{0} & \text{if } \boldsymbol{x} \in \operatorname{Int}\mathcal{C} \\ \boldsymbol{y} = -\alpha \frac{\boldsymbol{x}}{\|\boldsymbol{x}\|},\ \alpha \in \mathbb{R}_+ & \text{if } \boldsymbol{x} \in \operatorname{Bd}\mathcal{C} \end{cases}
\end{aligned}$$

For $\boldsymbol{x} = \boldsymbol{\lambda}_{\mathrm{T}}$ and $\boldsymbol{y} = \mathrm{D}(\mathbf{u})_{\mathrm{T}}$, we thus identify using Lemma 2 that

$$f^\star_{\mathrm{AC}}(\overline{\boldsymbol{\lambda}}, \overline{\mathrm{D}(\mathbf{u})})_{\mathrm{T}} = 0 \iff \text{(14a — 14b)}. \tag{17}$$

where $f^\star_{\mathrm{AC}}(\overline{\boldsymbol{\lambda}}, \overline{\mathrm{D}(\mathbf{u})})_{\mathrm{T}}$ denotes the $\mathfrak{t}(d)$ last components (tangential part) of $f^\star_{\mathrm{AC}}(\overline{\boldsymbol{\lambda}}, \overline{\mathrm{D}(\mathbf{u})})$. In the degenerate case where $\kappa_{\mu,\boldsymbol{\sigma}_0}(\lambda_{\mathrm{N}}) = 0$, we have $C = \{\mathbf{0}\}$ and $\mathcal{N}_{\mathcal{C}}(\boldsymbol{x} \in \mathcal{C}) = \mathbb{R}^{\mathfrak{t}(d)}$. We thus trivially obtain $\boldsymbol{x} = \Pi_{\mathcal{C}}(\boldsymbol{x} - \xi\boldsymbol{y}) \iff \boldsymbol{x} = \mathbf{0}$, the latter equality being what Equations (14a — 14b) boil down to for $\boldsymbol{x} = \boldsymbol{\lambda}_{\mathrm{T}}$ and $\boldsymbol{y} = \mathrm{D}(\mathbf{u})_{\mathrm{T}}$ when $\kappa_{\mu,\boldsymbol{\sigma}_0}(\lambda_{\mathrm{N}}) = 0$. We thus again retrieve the above equivalence (17).

□

Extended De Saxcé formulation Let $n \geq 2$. Let $\mathcal{K}^n_{\mu,\sigma_0}$ be the truncated version of the $\mathbf{SOC}\mathcal{K}^n_\mu$ already defined in (7),

$$\mathcal{K}^n_{\mu,\sigma_0} := \left\{(x_{\mathrm{N}}, \boldsymbol{x}_{\mathrm{T}}) \in \mathbb{R}_+ \times \mathbb{R}^{n-1}, \|\boldsymbol{x}_{\mathrm{T}}\| \leq \sigma_0 + \mu x_{\mathrm{N}}\right\}. \tag{18}$$

See Figure 2, right, for an illustration in the case when $n = 3$. Note that similarly to $\mathcal{K}^n_\mu$, the set $\mathcal{K}^n_{\mu,\sigma_0}$ is convex, and for $\sigma_0 = 0$ we recover $\mathcal{K}^n_{\mu,\sigma_0} = \mathcal{K}^n_\mu$.

Let us apply a similar change of variable to De Saxcé's [DSF98] on our symmetric velocity gradient tensor $\mathrm{D}(\mathbf{u})$, $\hat{\mathrm{D}}(\mathbf{u}) := \mathrm{D}(\mathbf{u}) + \sqrt{\frac{2}{d}}\mu|\operatorname{Dev}(\mathrm{D}(\mathbf{u}))|\mathbf{I}$. Using (13) and the linearity of the trace operator on the one hand, the linearity of the $()_{\mathrm{T}}$ operator and the fact that $\mathbf{I}_{\mathrm{T}} = \mathbf{0}$ on the other hand, we get

$$\hat{\mathrm{D}}(\mathbf{u})_{\mathrm{N}} = \mathrm{D}(\mathbf{u})_{\mathrm{N}} + \mu\|\mathrm{D}(\mathbf{u})_{\mathrm{T}}\| \tag{19a}$$

$$\hat{\mathrm{D}}(\mathbf{u})_{\mathrm{T}} = \mathrm{D}(\mathbf{u})_{\mathrm{T}}. \tag{19b}$$

Similarly to the modified solid velocity $\hat{\boldsymbol{u}} \in \mathbb{R}^d$ introduced in Section 3.2.1, which automatically lies in the polar cone $\mathcal{K}^d_{\frac{1}{\mu}}$ when $u_{\mathrm{N}} \geq 0$, our quantity $\overline{\hat{\mathrm{D}}(\mathbf{u})} \in \mathbb{R}^{1+dT}$ has an unchanged tangential component and a normal component that is modified such that $\overline{\hat{\mathrm{D}}(\mathbf{u})} \in \mathcal{K}^{\mathfrak{s}(d)}_{\frac{1}{\mu}}$ when $\mathrm{D}(\mathbf{u})_{\mathrm{N}} \geq 0$ (see Equivalence (22a)).

Definition 3. *Let us introduce the following extension of the De Saxcé function,*

$$\begin{array}{rccc} f^\star_{DS} & : & \mathbb{R}^{\mathfrak{s}(d)} \times \mathbb{R}^{\mathfrak{s}(d)} & \longrightarrow & \mathbb{R}^{\mathfrak{s}(d)} \\ & & (\overline{\boldsymbol{\lambda}}, \overline{\mathrm{D}(\mathbf{u})}) & \longmapsto & \Pi_{\mathcal{K}^{\mathfrak{s}(d)}_{\mu,\sigma_0}}\left(\overline{\boldsymbol{\lambda}} - \xi\overline{\hat{\mathrm{D}}(\mathbf{u})}\right) - \overline{\boldsymbol{\lambda}} \end{array} \tag{20}$$

where ξ is a positive real number.

Theorem 3. *The following equivalence holds,*

$$(\boldsymbol{\lambda}; \mathrm{D}(\mathbf{u})) \in \mathcal{DP}(\mu, \sigma_0) \iff f^\star_{DS}(\overline{\boldsymbol{\lambda}}, \overline{\mathrm{D}(\mathbf{u})}) = \mathbf{0}. \tag{21}$$

Corollary 1. *When $\sigma_0 = 0$, the rheology $\mathcal{DP}(\mu, \sigma_0)$ can be expressed as a Second-Order Cone Complementarity Problem (***SOCCP***),*

$$(\boldsymbol{\lambda}; \mathrm{D}(\mathbf{u})) \in \mathcal{DP}(\mu, 0) \iff \mathcal{K}_{\mu}^{s(d)} \ni \overline{\boldsymbol{\lambda}} \perp \overline{\hat{\mathrm{D}}(\mathbf{u})} \in \mathcal{K}_{\frac{1}{\mu}}^{s(d)},$$

where the $\perp$ notation refers to Euclidean orthogonality in $\mathbb{R}^{s(d)}$.

Proof. For the sake of brevity, we only prove Theorem 21 in the case $\sigma_0 > 0$. The case $\sigma_0 = 0$ and Corollary (1) reduce to the standard Signorini-Coulomb law and are dealt with, for instance, in [Cad09].

Again, given Theorem 1, it is enough to show that $f_{\mathrm{DS}}^{\star}(\overline{\boldsymbol{\lambda}}, \overline{\mathrm{D}(\mathbf{u})}) = \mathbf{0}$ if and only if $\left(\overline{\boldsymbol{\lambda}}; \overline{\mathrm{D}(\mathbf{u})}\right)$ satisfies Problem (14). Let us first notice that the following equivalences hold,

$$\overline{\hat{\mathrm{D}}(\mathbf{u})} \in \mathcal{K}_{\frac{1}{\mu}}^{s(d)} \iff \mathrm{D}(\mathbf{u})_{\mathrm{N}} \geq 0 \tag{22a}$$

$$\overline{\hat{\mathrm{D}}(\mathbf{u})} \in \mathrm{Bd}\,\mathcal{K}_{\frac{1}{\mu}}^{s(d)} \iff \mathrm{D}(\mathbf{u})_{\mathrm{N}} = 0 \tag{22b}$$

$$\text{and} \quad \overline{\hat{\mathrm{D}}(\mathbf{u})} = \mathbf{0} \iff \overline{\mathrm{D}(\mathbf{u})} = \mathbf{0}. \tag{22c}$$

Moreover, since $\sigma_0 > 0$ implies that $\kappa_{\mu,\boldsymbol{\sigma}_0}(\lambda_{\mathrm{N}}) > 0$, we can use Lemmas 1 and 2 to write Problem (14) equivalently as

$$(14) \iff \begin{cases} \overline{\boldsymbol{\lambda}} \in \mathcal{K}_{\mu,\sigma_0} & \\ \mathrm{D}(\mathbf{u})_{\mathrm{T}} = -\alpha \boldsymbol{\lambda}_{\mathrm{T}},\ \alpha \in \mathbb{R}_+ & \text{if } \|\boldsymbol{\lambda}_{\mathrm{T}}\| = \kappa_{\mu,\boldsymbol{\sigma}_0}(\lambda_{\mathrm{N}}) \\ \mathrm{D}(\mathbf{u})_{\mathrm{T}} = 0 & \text{if } \|\boldsymbol{\lambda}_{\mathrm{T}}\| < \kappa_{\mu,\boldsymbol{\sigma}_0}(\lambda_{\mathrm{N}}) \\ \mathrm{D}(\mathbf{u})_{\mathrm{N}} \geq 0 & \text{if } \lambda_{\mathrm{N}} = 0 \\ \mathrm{D}(\mathbf{u})_{\mathrm{N}} = 0 & \text{if } \lambda_{\mathrm{N}} > 0. \end{cases} \tag{23}$$

Now, from the projection theorem (9), we have

$$f_{\mathrm{DS}}^{\star}(\overline{\boldsymbol{\lambda}}, \overline{\mathrm{D}(\mathbf{u})}) = \mathbf{0} \iff \overline{\hat{\mathrm{D}}(\mathbf{u})} \in -\mathcal{N}_{\mathcal{K}_{\mu,\sigma_0}^{s(d)}}\left(\overline{\boldsymbol{\lambda}}\right). \tag{24}$$

Let us specify the form of the normal cone $\mathcal{N}_{\mathcal{C}}\left(\overline{\boldsymbol{\lambda}}\right)$ with $\mathcal{C} := \mathcal{K}_{\mu,\sigma_0}^{s(d)}$, for the four different cases of $\overline{\boldsymbol{\lambda}} \in \mathcal{C}$.

i. $\lambda_{\mathrm{N}} > 0$ and $\|\boldsymbol{\lambda}_{\mathrm{T}}\| < \kappa_{\mu,\boldsymbol{\sigma}_0}(\lambda_{\mathrm{N}})$, i.e., $\overline{\boldsymbol{\lambda}} \in \mathrm{Int}\,\mathcal{C}$. Then $\mathcal{N}_{\mathcal{C}}\left(\overline{\boldsymbol{\lambda}}\right) = \{\mathbf{0}\}$ and from (22c) we get

$$\overline{\hat{\mathrm{D}}(\mathbf{u})} \in -\mathcal{N}_{\mathcal{C}}\left(\overline{\boldsymbol{\lambda}}\right) \iff \overline{\boldsymbol{\lambda}} \in \mathcal{C},\ \overline{\mathrm{D}(\mathbf{u})} = \mathbf{0}.$$

ii. $\lambda_{\mathrm{N}} > 0$ and $\|\boldsymbol{\lambda}_{\mathrm{T}}\| = \kappa_{\mu,\boldsymbol{\sigma}_0}(\lambda_{\mathrm{N}})$, i.e., $\overline{\boldsymbol{\lambda}}$ lies on the smooth conical part of $\mathrm{Bd}\,\mathcal{C}$. The outward normal to $\mathcal{C}$ at $\overline{\boldsymbol{\lambda}}$ reads $\mathbf{n}_{\mathcal{C}}(\overline{\boldsymbol{\lambda}}) = \frac{1}{\sqrt{1+\mu^2}}\left(-\mu; \frac{\boldsymbol{\lambda}_{\mathrm{T}}}{\|\boldsymbol{\lambda}_{\mathrm{T}}\|}\right)$, and thus we have $\mathcal{N}_{\mathcal{C}}\left(\overline{\boldsymbol{\lambda}}\right) = \left\{\alpha\left(-\mu; \frac{\boldsymbol{\lambda}_{\mathrm{T}}}{\|\boldsymbol{\lambda}_{\mathrm{T}}\|}\right), \alpha \in \mathbb{R}_+\right\} \subset -\mathrm{Bd}\,\mathcal{K}_{\frac{1}{\mu}}^{s(d)}$. Using (22b) and (19b), we get

$$\overline{\hat{\mathrm{D}}(\mathbf{u})} \in -\mathcal{N}_{\mathcal{C}}\left(\overline{\boldsymbol{\lambda}}\right) \iff \begin{cases} \overline{\boldsymbol{\lambda}} \in \mathcal{C} \\ \mathrm{D}(\mathbf{u})_{\mathrm{N}} = 0 \\ \mathrm{D}(\mathbf{u})_{\mathrm{T}} = -\alpha \boldsymbol{\lambda}_{\mathrm{T}},\ \alpha \in \mathbb{R}_+. \end{cases}$$

iii. $\lambda_{\mathrm{N}} = 0$ and $\|\boldsymbol{\lambda}_{\mathrm{T}}\| < \kappa_{\mu,\boldsymbol{\sigma}_0}(\lambda_{\mathrm{N}})$, i.e., $\overline{\boldsymbol{\lambda}}$ lies on the smooth planar base of $\mathrm{Bd}\,\mathcal{C}$ We have $\mathbf{n}_{\mathcal{C}}(\overline{\boldsymbol{\lambda}}) = (-1; \mathbf{0})$ and then $\mathcal{N}_{\mathcal{C}}\left(\overline{\boldsymbol{\lambda}}\right) = \{\alpha(-1; \mathbf{0}), \alpha \in \mathbb{R}_+\}$. Thus,

$$\overline{\hat{\mathrm{D}}(\mathbf{u})} \in -\mathcal{N}_{\mathcal{C}}\left(\overline{\boldsymbol{\lambda}}\right) \iff \overline{\boldsymbol{\lambda}} \in \mathcal{C},\ \mathrm{D}(\mathbf{u})_{\mathrm{T}} = 0 \text{ and } \mathrm{D}(\mathbf{u})_{\mathrm{N}} \geq 0.$$

iv. $\lambda_{\mathrm{N}} = 0$ and $\|\boldsymbol{\lambda}_{\mathrm{T}}\| = \kappa_{\mu,\boldsymbol{\sigma}_0}(\lambda_{\mathrm{N}})$, i.e., $\overline{\boldsymbol{\lambda}}$ lies on the nonsmooth circular part of $\mathrm{Bd}\,\mathcal{C}$. Then $\mathcal{N}_{\mathcal{C}}\left(\overline{\boldsymbol{\lambda}}\right) = -\mathcal{K}^{s(d)}_{\frac{1}{\mu}} \cap \left\{\boldsymbol{\gamma} \in \mathbb{R}^{s(d)}, \boldsymbol{\gamma}_{\mathrm{T}} = \alpha\boldsymbol{\lambda}_{\mathrm{T}},\ \alpha \in \mathbb{R}_+\right\}$. Again, from (22a) and (19b),

$$\overline{\hat{\mathrm{D}}\left(\mathbf{u}\right)} \in -\mathcal{N}_{\mathcal{C}}\left(\overline{\boldsymbol{\lambda}}\right) \iff \overline{\boldsymbol{\lambda}} \in \mathcal{C},\ \mathrm{D}(\mathbf{u})_{\mathrm{N}} \geq 0 \text{ and } \mathrm{D}\left(\mathbf{u}\right)_{\mathrm{T}} = -\alpha\boldsymbol{\lambda}_{\mathrm{T}},\ \alpha \in \mathbb{R}_+.$$

Finally, it is straightforward to see that the union of the four cases i, ii, iii, iv exactly amounts to our conditions derived in (23).

□

4 Creeping flow

4.1 The continuous setting

In this first section we assume that the flow is slow enough for its inertia to be neglected, and solve for its steady state. This case is relevant since the structure of the equations for each time-step of the fully dynamic case will be similar (see Section 5).

Let us consider a domain $\Omega \subset \mathbb{R}^d$ and decompose its boundary as $\partial\Omega := B_D \cup B_N$, with Dirichlet boundary conditions on B_D and homogeneous Neumann on B_N,

$$\mathbf{u} = \mathbf{u}_D \qquad \text{on } B_D \tag{25a}$$

$$\mathrm{D}^b(\mathbf{u})\,\mathbf{n}_\Omega = \mathbf{0} \qquad \text{on } B_N \tag{25b}$$

where $\mathbf{n}_\Omega$ is the outward-pointing normal to Ω on each point of its boundary.

Moreover, let $\boldsymbol{\sigma}_{ext}$ gather all external stresses applied onto the Neumann boundary of the domain. We thus have

$$-\boldsymbol{\lambda}\,\mathbf{n}_\Omega = \boldsymbol{\sigma}_{ext}\,\mathbf{n}_\Omega \qquad \text{on } B_N \tag{26}$$

Conservation of momentum gives

$$-\nabla\cdot\Bigg[\underbrace{2\eta\,\mathrm{D}^b(\mathbf{u}) - \boldsymbol{\lambda}}_{=\boldsymbol{\sigma}_{tot}}\Bigg] = \rho g \mathbf{e}_g \quad \text{ on } \Omega \tag{27}$$

with $\mathbf{e}_g$ the "down" unit vector.

Dimensionless equations Let L be a characteristic dimension of the flow. We define $U := \sqrt{gL}$ the characteristic velocity and $P := \rho g L$ the characteristic pressure of the flow. We consider dimensionless differential operators defined through $\tilde{\nabla} := L\,\nabla$. We furthermore introduce two dimensionless numbers, the Reynolds number $\mathrm{Re} := \frac{\rho U L}{\eta}$ and the Bingham number $\mathrm{Bi} := \frac{\sigma_0}{\rho g L} = \frac{\sigma_0}{P}$.

Considering the dimensionless quantities $\tilde{\mathbf{u}} := \frac{1}{U}\mathbf{u}$, $\tilde{\boldsymbol{\tau}} := \frac{1}{P}\boldsymbol{\tau}$, $\tilde{\boldsymbol{\lambda}} := \frac{1}{P}\boldsymbol{\lambda}$, and $\tilde{\mathbf{u}}_D := \frac{1}{U}\mathbf{u}_D$, Equations (25 — 27) can be nondimensionalized as

$$\begin{cases} -\tilde{\nabla}\cdot\left[\frac{2}{\mathrm{Re}}\widetilde{\mathrm{D}^b}\left(\tilde{\mathbf{u}}\right) - \tilde{\boldsymbol{\lambda}}\right] &=& \mathbf{e}_g & \text{on } \Omega \\ \tilde{\mathbf{u}} &=& \tilde{\mathbf{u}}_D & \text{on } B_D \\ \widetilde{\mathrm{D}^b}\left(\tilde{\mathbf{u}}\right)\,\mathbf{n}_\Omega &=& \mathbf{0} & \text{on } B_N \\ -\tilde{\boldsymbol{\lambda}}\,\mathbf{n}_\Omega &=& \tilde{\boldsymbol{\sigma}}_{ext}\,\mathbf{n}_\Omega & \text{on } B_N, \end{cases} \tag{28}$$

with the dimensionless rheology

$$\left(\tilde{\boldsymbol{\lambda}}; \tilde{\mathrm{D}}\left(\tilde{\mathbf{u}}\right)\right) \in \mathcal{DP}\left(\mu, \mathrm{Bi}\right). \tag{29}$$

Proof. By noting that $\tilde{\mathrm{D}}(\tilde{\mathbf{u}}) = \frac{L}{U}\mathrm{D}(\mathbf{u})$ and $\frac{2\eta U}{L^2\rho g} = \frac{2}{\mathrm{Re}}$, Equations (28) can be obtained from (25 — 27) by direct calculation. As for the dimensionless granular rheology (29), it directly follows from (14) by noting that $\frac{1}{P}\kappa_{\mu,\boldsymbol{\sigma}_0}(\lambda_{\mathrm{N}}) = \kappa_{\mu,\mathrm{Bi}}(\tilde{\lambda}_{\mathrm{N}})$, and that, again, complementarity is insensitive to positive scaling factors. □

In the remainder of this article, unless otherwise mentioned we shall use the dimensionless quantities and omit the tildes. In particular, from now we shall use the notation $(\boldsymbol{\lambda}; \mathrm{D}(\mathbf{u})) \in \mathcal{DP}(\mu, \mathrm{Bi})$ for denoting our granular rheology.

4.2 Variational formulation

Let $H^1(\Omega)^d$ be the usual Sobolev space containing square-integrable functions from $\mathbb{R}^d \times \mathbb{R}$ to $\mathbb{R}^d$, with square-integrable gradients. As in [Sar15, Appendix A], we introduce the subspace $V(\mathbf{u}_D)$ of $H^1(\Omega)^d$ for which the Dirichlet boundary condition (25a) is satisfied, i.e.,

$$V(\mathbf{u}_D) = \{\mathbf{u} \in H^1(\Omega)^d;\ \mathbf{u} = \mathbf{u}_D \text{ on } B_D\}$$

and the subspace $V(\mathbf{0})$ of $H^1(\Omega)^d$ for which the homogeneous Dirichlet boundary condition is satisfied, i.e.,

$$V(\mathbf{0}) = \{\mathbf{v} \in H^1(\Omega)^d;\ \mathbf{v} = \mathbf{0} \text{ on } B_D\}.$$

Let $T(\Omega)$ be the space of square-integrable symmetric tensor fields on Ω.

Proposition 1. *A weak form of System (28 — 29) amounts to finding* $\mathbf{u} \in V(\mathbf{u}_D)$, $\boldsymbol{\lambda} \in T(\Omega)$, *and* $\boldsymbol{\gamma} \in T(\Omega)$, *such that*

$$\begin{cases} a(\mathbf{u}, \mathbf{v}) = b(\boldsymbol{\lambda}, \mathbf{v}) + l(\mathbf{v}) & \forall \mathbf{v} \in V(\mathbf{0}) \quad (30a) \\ m(\boldsymbol{\gamma}, \boldsymbol{\tau}) = b(\boldsymbol{\tau}, \mathbf{u}) & \forall \boldsymbol{\tau} \in T(\Omega) \quad (30b) \\ (\boldsymbol{\lambda}; \boldsymbol{\gamma}) \in \mathcal{DP}(\mu, \mathrm{Bi}), & (30c) \end{cases}$$

where $\forall \mathbf{x}, \mathbf{y} \in H^1(\Omega)^d$ *and* $\forall \boldsymbol{\sigma}, \boldsymbol{\tau} \in T(\Omega)$, $a(\mathbf{x}, \mathbf{y})$ *and* $m(\boldsymbol{\sigma}, \boldsymbol{\tau})$ *are the symmetric positive-definite bilinear forms on* $H^1(\Omega)^d \times H^1(\Omega)^d$ *and* $T(\Omega) \times T(\Omega)$, *respectively,*

$$a(\mathbf{x}, \mathbf{y}) = \frac{2}{\mathrm{Re}} \int_\Omega \mathrm{D}^0(\mathbf{x}) : \mathrm{D}^0(\mathbf{y}) + \frac{b}{d} (\nabla \cdot \mathbf{x})(\nabla \cdot \mathbf{y})$$
$$m(\boldsymbol{\sigma}, \boldsymbol{\tau}) = \int_\Omega \boldsymbol{\sigma} : \boldsymbol{\tau},$$

$b(\boldsymbol{\tau}, \mathbf{x})$ *is the bilinear form on* $T(\Omega) \times H^1(\Omega)^d$,

$$b(\boldsymbol{\tau}, \mathbf{x}) = \int_\Omega \mathrm{D}(\mathbf{x}) : \boldsymbol{\tau},$$

and $l(\mathbf{x})$ *is the linear form on* $H^1(\Omega)^d$,

$$l(\mathbf{x}) = \int_\Omega \mathbf{e}_g \cdot \mathbf{x} - \int_{B_N} (\boldsymbol{\sigma}_{ext}\, \mathbf{n}_\Omega) \cdot \mathbf{x}$$

Proof. First, let us consider the stress boundary condition (26). One solution would be to enfore it strongly, by discretizing $\boldsymbol{\lambda}$ over the subspace of $T(\Omega)$ which statisfy (26). However, this may lead to difficulties in the discretization of the $\mathcal{DP}(\mu, \mathrm{Bi})$ rheology. In our proposed implementation, we chose instead to allow in the integration of the term $\nabla \cdot \boldsymbol{\sigma}_{tot}$ for a possibly non-zero jump $[\![\boldsymbol{\sigma}_{tot}]\!]$ of the stress on B_N.

Let us now derive the variational formulation for System (28). We assume $\mathbf{u} \in V(\mathbf{u}_D)$, and $\boldsymbol{\lambda} \in T(\boldsymbol{\sigma}_{ext})$, and let $\mathbf{v} \in V(\mathbf{0})$ be a test function. In this setting, multiplying both sides of (28) by $\mathbf{v}$ and integrating over Ω yields

$$-\int_\Omega \nabla \cdot \left(\frac{2}{\mathrm{Re}} \mathrm{D}^b(\mathbf{u}) - \boldsymbol{\lambda} \right) \cdot \mathbf{v} + \int_{B_N} [\![\boldsymbol{\sigma}_{tot}]\!] \mathbf{n}_\Omega \cdot \mathbf{v} = \int_\Omega \mathbf{e}_g \cdot \mathbf{v}. \quad (31)$$

Using the Green formula with the (25b) boundary condition for $\mathbf{u}$ and the homogeneous Dirichlet condition for $\mathbf{v}$, we have

$$\begin{aligned} -\int_\Omega \left(\nabla\cdot\frac{2}{\mathrm{Re}}\,\mathrm{D}^b(\mathbf{u})\right)\cdot\mathbf{v} &= \int_\Omega \frac{2}{\mathrm{Re}}\,\mathrm{D}^b(\mathbf{u}):\mathrm{D}(\mathbf{v}) \\ &= \frac{2}{\mathrm{Re}}\int_\Omega \mathrm{D}^0(\mathbf{u}):\mathrm{D}^0(\mathbf{v}) + \frac{b}{d}\,(\nabla\cdot\mathbf{v})\,(\nabla\cdot\mathbf{u}) \\ &= a(\mathbf{u},\mathbf{v}) \end{aligned} \tag{32}$$

and

$$\begin{aligned} \int_\Omega \nabla\cdot[\boldsymbol{\lambda}]\cdot\mathbf{v} + \int_{B_N} [\![\boldsymbol{\sigma}_{tot}]\!]\mathbf{n}_\Omega\cdot\mathbf{v} &= \int_{B_N} ([\![\boldsymbol{\sigma}_{tot}]\!]+\boldsymbol{\lambda})\,\mathbf{n}_\Omega\cdot\mathbf{v} - b(\boldsymbol{\lambda},\mathbf{v}) \\ &= -\int_{B_N} \boldsymbol{\sigma}_{ext}\mathbf{n}_\Omega\cdot\mathbf{v} - b(\boldsymbol{\lambda},\mathbf{v}). \end{aligned} \tag{33}$$

By combining (31 – 33) and the definition of l, we retrieve (30a).

Let us now focus on the rheology $\mathcal{DP}\,(\mu,\mathrm{Bi})$ given in (29), which contains inequalities that cannot be put directly under weak form. To circumvent this difficulty, we introduce an auxiliary variable $\boldsymbol{\gamma}\in T(\Omega)$ that weakly satisfies $\boldsymbol{\gamma}=\mathrm{D}(\mathbf{u})$, i.e.,

$$\int_\Omega \mathrm{D}(\mathbf{u}):\boldsymbol{\tau} = \int_\Omega \boldsymbol{\gamma}:\boldsymbol{\tau} \quad \forall\boldsymbol{\tau}\in T(\Omega), \tag{34}$$

which is exactly equation (30b). We can thus express the rheology $\mathcal{DP}\,(\mu,\mathrm{Bi})$ under the weak form as (30b —30c). □

4.3 Discretization by Finite Elements (FEM)

4.3.1 Discretization of the symmetric tensor fields

For the discretization of the space $T(\Omega)$, we shall make use of Lagrange FEM, that is all symmetric tensor fields will be expressed as functions of Ω, built as an interpolation of their values at the n degrees of freedom x_i.

Let Q_h be a finite-dimensional subspace of $L_2(\Omega)$ of dimension n. Let $(\alpha_i)_{1\le i\le n}$ be a basis of Q_h, such that $\alpha_i(x_j)=\delta_{i,j}$. Let $(\mathbf{e}_j)_{1\le j\le \mathfrak{s}(d)}$ be the canonical basis for $\mathbb{R}^{\mathfrak{s}(d)}$. Then $\left(\boldsymbol{\alpha}_k^{\mathfrak{s}(d)}\right)_{1\le k\le \mathfrak{s}(d)\,n}$, defined as

$$\forall x\in\Omega,\quad \boldsymbol{\alpha}^{\mathfrak{s}(d)}_{\mathfrak{s}(d)\,(i-1)+j}(x) := \alpha_i(x)\,\mathbf{e}_j \qquad \text{for } 1\le i\le n \quad\text{and}\quad 1\le j\le \mathfrak{s}(d)$$

is a natural basis for $Q_h^{\mathfrak{s}(d)}$. Finally, we may build a finite subspace $T_h\subset T(\Omega)$ from the basis $(\boldsymbol{\sigma}_k)_{1\le k\le \mathfrak{s}(d)\,n}$ defined as

$$\forall x\in\Omega,\quad \boldsymbol{\sigma}_{\mathfrak{s}(d)\,(i-1)+j}(x) := \alpha_i(x)\chi(\mathbf{e}_j) \qquad \text{for } 1\le i\le n \quad\text{and}\quad 1\le j\le \mathfrak{s}(d)$$

where our orthogonal isomorphism χ from $\mathbb{R}^{\mathfrak{s}(d)}$ to S_d has been formerly introduced in Definition 1. We have the following relationship between the two bases $\left(\boldsymbol{\alpha}^{\mathfrak{s}(d)}\right)_k$ and $(\boldsymbol{\sigma})_k$,

$$\forall x\in\Omega,\quad \chi\left(\boldsymbol{\alpha}_k^{\mathfrak{s}(d)}(x)\right) = \boldsymbol{\sigma}_k(x) \qquad \text{for } 1\le k\le \mathfrak{s}(d)\,n. \tag{35}$$

Now, for $\boldsymbol{\lambda}$ and $\boldsymbol{\gamma}$ two symmetric tensor fields in $T(\Omega)$, let $\boldsymbol{\lambda}_h,\boldsymbol{\gamma}_h\in T_h$ be their corresponding discretized functions built by interpolation at the n degrees of freedom x_i. Let $\boldsymbol{\Lambda}_h$ and $\boldsymbol{\Gamma}_h$ be the vectors of the (scalar) coefficients of the decomposition of $\boldsymbol{\lambda}_h$ and $\boldsymbol{\gamma}_h$, respectively, in the basis $(\boldsymbol{\sigma})_k$. That is, $\boldsymbol{\lambda}_h(x)=\sum_k \boldsymbol{\Lambda}_{h,k}\boldsymbol{\sigma}_k(x)$, and $\boldsymbol{\gamma}_h(x)=\sum_k \boldsymbol{\Gamma}_{h,k}\boldsymbol{\sigma}_k(x)$. Note that using (35), functions $\overline{\boldsymbol{\lambda}_h}$ and $\overline{\boldsymbol{\gamma}_h}$ decompose on the basis $\left(\boldsymbol{\alpha}^{\mathfrak{s}(d)}\right)_k$ with exactly the same coefficients, that is $\overline{\boldsymbol{\lambda}_h}(x)=\sum_k \boldsymbol{\Lambda}_{h,k}\boldsymbol{\alpha}_k^{\mathfrak{s}(d)}(x)$, and $\overline{\boldsymbol{\gamma}_h}(x)=\sum_k \boldsymbol{\Gamma}_{h,k}\boldsymbol{\alpha}_k^{\mathfrak{s}(d)}(x)$. Thus,

since $\boldsymbol{\alpha}^{\mathfrak{s}(d)}_{\mathfrak{s}(d)\,(m-1)+j}(x_i) = \delta_{i,m}\,\mathbf{e}_j$, each vector of $\mathfrak{s}(d)$ coefficients $\boldsymbol{\Lambda}_h[i] \coloneqq \{\boldsymbol{\Lambda}_{h,\mathfrak{s}(d)\,(i-1)+j}, 1 \leq j \leq \mathfrak{s}(d)\}$ corresponds to the value $\overline{\boldsymbol{\lambda}_h}(x_i)$, and the decomposition of $\overline{\boldsymbol{\lambda}_h}(x)$ on the scalar basis $(\alpha)_i$ reads $\overline{\boldsymbol{\lambda}_h}(x) = \sum_i \boldsymbol{\Lambda}_h[i]\,\alpha_i(x)$. Similarly, we have $\boldsymbol{\Gamma}_h[i] = \overline{\boldsymbol{\gamma}_h}(x_i)$ and $\overline{\boldsymbol{\gamma}_h}(x) = \sum_i \boldsymbol{\Gamma}_h[i]\,\alpha_i(x)$.

From (21) and using the aforementioned properties, we may express our discrete granular rheology at each degree of freedom $x_{i,1\leq i\leq n}$ as

$$(\boldsymbol{\lambda}_h(x_i);\boldsymbol{\gamma}_h(x_i)) \in \mathcal{DP}\,(\mu,\mathrm{Bi}) \iff f^\star_{\mathrm{DS}}\,(\boldsymbol{\Lambda}_h[i],\boldsymbol{\Gamma}_h[i]) = \mathbf{0}. \tag{36}$$

4.3.2 Discretization of the (bi)linear forms

Let $U_h \subset H^1(\Omega)^d$ be a finite-dimensional vectorial space, and $V_h \subset U_h$ its subspace satisfying the Dirichlet boundary conditions

$$V_h(\mathbf{u}_D) \coloneqq \{\mathbf{v}_h \in U_h, \mathbf{v}_h = \mathbf{u}_{Dh} \text{ on } B_D\}\,,$$

where $\mathbf{u}_{Dh}$ is the approximated (discrete) value of $\mathbf{u}_D$ on the FEM mesh. Let $\mathbf{u}^*_{Dh} \in U_h$ be the unique function such that for any $\mathbf{u}_h \in V_h(\mathbf{u}_D), \mathbf{u}^*_{Dh} = \mathbf{u}_h - \Pi_{V_h(\mathbf{0})}(\mathbf{u}_h)$, where we recall that $\Pi_{\mathcal{C}}$ is the orthogonal projection operator onto the convex set $\mathcal{C}$.

Unlike for the space T_h, here we make no specific assumption regarding the structure of $V_h(\mathbf{u}_D)$ or the construction of a corresponding base. Let $\mathfrak{v} \coloneqq \dim V_h$. Given $(\boldsymbol{v}_i)_{1\leq i\leq \mathfrak{v}}$ a basis of $V_h(\mathbf{0})$, we denote by A, B, and M the matrices corresponding to the decomposition of the bilinear forms a, b, and m respectively, and by $\mathbf{l}$ the vector corresponding to the decomposition of the linear form l. More precisely, we have $A_{i,j} = a(\boldsymbol{v}_i,\boldsymbol{v}_j)$, $M_{k,\ell} = m(\boldsymbol{\sigma}_k,\boldsymbol{\sigma}_\ell)$, $B_{k,j} = b(\boldsymbol{\sigma}_k,\boldsymbol{v}_j)$ and $\mathbf{l}_j = l(\boldsymbol{v}_j)$. Similarly, let $\mathbf{U}_h$ be the vector of scalar coefficients corresponding to the decomposition of $\mathbf{u}_h$. We have, $\forall x \in \Omega$, $\mathbf{u}_h(x) = \sum_{1\leq i\leq \mathfrak{v}} \mathbf{U}_{h,i}\,\boldsymbol{v}_i(x) + \mathbf{u}^*_{Dh}(x)$.

4.3.3 FEM discrete system

Finally, at this point the discrete version of Equations (30a — 30c) reads

$$\text{Find } \mathbf{u}_h \in V_h(\mathbf{u}_D),\ (\boldsymbol{\lambda}_h,\boldsymbol{\gamma}_h) \in T_h^2, \quad \begin{cases} A\,\mathbf{U}_h = B^{\mathsf{T}}\,\boldsymbol{\Lambda}_h + \underbrace{\mathbf{l} - \mathbf{a}_D}_{\mathbf{l}_{tot}} & \text{(37a)} \\ M\,\boldsymbol{\Gamma}_h = B\,\mathbf{U}_h + \mathbf{k} & \text{(37b)} \\ (\boldsymbol{\lambda}_h;\boldsymbol{\gamma}_h) \in \mathcal{DP}\,(\mu,\mathrm{Bi}) & \text{(37c)} \end{cases}$$

where for $1 \leq i \leq \mathfrak{v}$, $\mathbf{a}_{D,i} = a(\mathbf{u}^*_{Dh},\boldsymbol{v}_i)$ and for $1 \leq k \leq \mathfrak{s}(d)\,n$, $\mathbf{k}_k = b(\boldsymbol{\sigma}_k,\mathbf{u}^*_{Dh})$.

4.3.4 Discretization of the rheology on quadrature points

In the discrete case, the non-convex rheology $\mathcal{DP}\,(\mu,\mathrm{Bi})$ will not be able to be satisfied at every point $x \in \Omega$, since values of the functions $\boldsymbol{\lambda}_h$ and $\boldsymbol{\gamma}_h$ at intermediate points will be reconstructed by interpolation of values at the degrees of freedom x_i. We shall thus restrict ourselves to a discrete number of points $\breve{x}_j$ on which to enforce $(\boldsymbol{\lambda}_h(\breve{x}_j);\boldsymbol{\gamma}_h(\breve{x}_j)) \in \mathcal{DP}\,(\mu,\mathrm{Bi})$. The remaining question is how to perform a good choice for this set of points $\breve{x}_j$. In the sequel we shall see that this choice has a direct impact onto the final form of the system to be solved, and thus on both the physical relevance of the discrete problem and the practical performance of available solving methods.

Discretization on Q_h's Lagrange degrees of freedom One obvious choice for $(\breve{x})_j$ is to consider the n degrees of freedom x_i themselves, which served to define the $(\alpha)_i$ basis and thus the finite-dimensional spaces Q_h and T_h. This way, using (36) we may replace (37c) with

$$f^\star_{\mathrm{DS}}\,(\boldsymbol{\Lambda}_h[i],\boldsymbol{\Gamma}_h[i]) = \mathbf{0} \quad \text{for} \quad 1 \leq i \leq n.$$

Since A and M are positive-definite, we may first eliminate the velocity variable $\mathbf{U}_h$ from (37a), and then get a linear relationship between $\mathbf{\Lambda}_h$ and $\mathbf{\Gamma}_h$ from (37b), $\mathbf{\Gamma}_h \propto M^{-1}W\mathbf{\Lambda}_h$ where $W = BA^{-1}B^\top$. Apart from the presence of the matrix M which yields a modified Delassus operator $\tilde{W} \coloneqq M^{-1}W$, we have thus obtained a system which is very similar to the one appearing in discrete contact mechanics, and for which a plethora of efficient solving methods exist [Cad09]. However, the presence of the matrix M breaks the symmetry of the operator $\tilde{W}$ (M and W do not commute in the general case). The discrete system (37) therefore lacks a fundamental symmetry property, which is key not only to guarantee physical consistency of our model, but also to design an efficient numerical solver.

From a physical point of view, such an asymmetry in our discrete frictional contact law typically implies that the maximum dissipation principle cannot be satisfied, meaning that some anisotropy is artificially introduced through the discretization.

From a purely numerical point of view, symmetry of the Delassus operator is not necessarily a prerequisite to common numerical solvers, but in our case it proves to be highly desirable for coming up with a tractable solving method. Indeed, among scalable available solvers, we basically have the choice between operator-splitting algorithms (such as the well-known nonsmooth contact dynamics (NSCD) method [JAJ98]), and optimization-based algorithms (e.g. [RA05, Cad09]). On the one hand, operator-splitting methods do not assume $\tilde{W}$ be symmetric, yet for efficiency purposes they require the explicit knowledge of $\tilde{W}$, especially when large systems are involved as it is the case here. In our case A^{-1} is dense, and so is $\tilde{W}$. Making such an explicit assembly thus turns out to be intractable. On the other hand, optimization-based methods do not require the explicit assembly of $\tilde{W}$, however they heavily rely upon its symmetry so as to identify $\mathbf{\Gamma}_h$ as the gradient of a quadratic function in $\mathbf{\Lambda}_h$ with Hessian $\tilde{W}$.

For these two reasons, we choose to discretize our constraints on an alternative set of points $(\breve{x})_j$ that will allow us to eliminate the matrix M and thus retrieve symmetry of $\tilde{W}$. This way we shall both recover physical consistency of our model, and benefit from efficient optimization-based solving methods.

Discretization on quadrature points As we are using a Lagrange FEM discretization of the space $T(\Omega)$ with polynomial interpolating bases, each integral $M_{k,\ell} = \int \boldsymbol{\sigma}_k : \boldsymbol{\sigma}_\ell$ can be computed exactly using Gaussian quadrature[3], i.e., as $\sum_q w_q \, (\boldsymbol{\sigma}_k(\hat{x}_q) : \boldsymbol{\sigma}_\ell(\hat{x}_q))$ where the $\hat{x}_{q,1\le j\le n_Q}$ are the so-called quadrature points and w_q their corresponding weights. As shown below, defining the set $(\breve{x})_q$ as the set of quadrature points $\hat{x}_q$ allows us to retrieve a symmetric Delassus operator.

Recall that for $\boldsymbol{\lambda}$ a symmetric tensor field in $T(\Omega)$, $\boldsymbol{\lambda}_h \in T_h$ corresponds to its discretized version interpolating the values at the n degrees of freedom x_m, with $\overline{\boldsymbol{\lambda}_h}(x_m) = \mathbf{\Lambda}_h[m]$. Let R be the $(\mathfrak{s}(d)\, n_Q \times \mathfrak{s}(d)\, n)$ matrix mapping those $\mathbf{\Lambda}_h[m]$ to the interpolated values $\overline{\boldsymbol{\lambda}_h}(\breve{x}_q)$ at the quadrature points $\breve{x}_q$. That is, R is such that

$$\breve{\mathbf{\Lambda}}_h = R\mathbf{\Lambda}_h,$$

where $\breve{\mathbf{\Lambda}}_h$ is the vector of size $\mathfrak{s}(d)\, n_Q$ concatenating the n_Q vector values $\breve{\mathbf{\Lambda}}_h[q] \coloneqq \overline{\boldsymbol{\lambda}_h}(\breve{x}_q)$ for $1 \le q \le n_Q$, and $\mathbf{\Lambda}_h$ the vector of size $\mathfrak{s}(d)\, n$ concatenating the n vector values $\mathbf{\Lambda}_h[m] = \overline{\boldsymbol{\lambda}_h}(x_m)$ for $1 \le m \le n$.

Matrix R contains $n_Q \times n$ square blocks $\mathfrak{R}_{q,j}$ of size $\mathfrak{s}(d) \times \mathfrak{s}(d)$ with $\mathfrak{R}_{q,j} = \alpha_j(\breve{x}_q)\, I_{\mathfrak{s}(d)}$ for all $1 \le q \le n_Q$ and $1 \le j \le n$, where $I_s(d)$ is the $\mathfrak{s}(d) \times \mathfrak{s}(d)$ identity block. This translates into the following elementwise expression

$$R_{(q-1)\mathfrak{s}(d)+p,(j-1)\mathfrak{s}(d)+\ell} = \alpha_j(\breve{x}_q)\delta_{p,\ell} \quad \text{for} \quad 1 \le p, \ell \le \mathfrak{s}(d).$$

[3] Of course each coefficient $M_{k,\ell}$ may alternatively be evaluated by direct integration, since primitives of the integrand are easily calculable. However, the quadrature technique is mentioned here as it provides a judicious set of points on which to discretize our rheology.

Property 3. *Let* $\breve{\mathbf{\Lambda}}_h := R\mathbf{\Lambda}_h$ *and* $\breve{\mathbf{\Gamma}}_h := R\mathbf{\Gamma}_h$*, and* $R^\dagger$ *the Moore-Penrose pseudoinverse of* R*. Then Equations (30a — 30c) can be discretized as*

$$\text{Find } \mathbf{U}_h \in \mathbb{R}^{\mathfrak{v}},\ \breve{\mathbf{\Lambda}}_h, \breve{\mathbf{\Gamma}}_h \in \mathbb{R}^{\mathfrak{s}(d)\,n_Q},\ \begin{cases} A\,\mathbf{U}_h = B^\top R^\dagger \breve{\mathbf{\Lambda}}_h + \mathbf{l}_{tot} & \text{(38a)} \\ \breve{\mathbf{\Gamma}}_h = {R^\dagger}^\top B\,\mathbf{U}_h + {R^\dagger}^\top \mathbf{k}_{tot} & \text{(38b)} \\ \forall 1 \le q \le n_Q, \quad f^\star_{DS}\left(\breve{\mathbf{\Lambda}}_h[q], \breve{\mathbf{\Gamma}}_h[q]\right) = \mathbf{0}. & \text{(38c)} \end{cases}$$

Proof. First, it is noteworthy that matrix M may be decomposed as $M = R^T S R$, where S is a $(\mathfrak{s}(d)\,n_Q \times \mathfrak{s}(d)\,n_Q)$ diagonal matrix mapping the diagonal weight block $\mathfrak{S}_{q,q} := 2\,w_q\,I_{\mathfrak{s}(d)}$ to each quadrature point q, that is for all $1 \le p \le n_Q$ and $1 \le q \le n_Q$,

$$S_{(p-1)\mathfrak{s}(d)+k,(q-1)\mathfrak{s}(d)+\ell} = 2\,\delta_{p,q}\,\delta_{k,\ell}\,w_q \quad \text{for} \quad 1 \le k, \ell \le \mathfrak{s}(d).$$

Indeed, for all $1 \le i, j \le n$ and for all $1 \le k, \ell \le n$, let $r := (i-1)\mathfrak{s}(d)+k$ and $c := (j-1)\mathfrak{s}(d)+\ell$. Using the quadrature rule, we have

$$\begin{aligned} M_{r,c} &= \sum_{q=1}^{n_Q} w_q\ (\boldsymbol{\sigma}_r(\breve{x}_q) : \boldsymbol{\sigma}_c(\breve{x}_q)) \\ &= 2\sum_{q=1}^{n_Q} w_q\ \left(\overline{\boldsymbol{\sigma}}_r(\breve{x}_q)^\top \overline{\boldsymbol{\sigma}}_c(\breve{x}_q)\right) \qquad \text{from (11)} \\ &= 2\sum_{q=1}^{n_Q} w_q\ \left(\alpha_i(\breve{x}_q)\mathbf{e}_k^\top \alpha_j(\breve{x}_q)\mathbf{e}_\ell\right) \\ &= 2\sum_{q=1}^{n_Q} w_q\ \left(\alpha_i(\breve{x}_q)\,\alpha_j(\breve{x}_q)\delta_{k,\ell}\right) \\ &= 2\sum_{q=1}^{n_Q}\sum_{p=1}^{\mathfrak{s}(d)} w_q\ \left(\alpha_i(\breve{x}_q)\,\alpha_j(\breve{x}_q)\delta_{k,p}\delta_{p,l}\right) \\ &= \sum_{q=1}^{n_Q}\sum_{p=1}^{\mathfrak{s}(d)} S_{(q-1)\mathfrak{s}(d)+p,(q-1)\mathfrak{s}(d)+p}\ \left(R_{(q-1)\mathfrak{s}(d)+p,r} R_{(q-1)\mathfrak{s}(d)+p,c}\right) \end{aligned}$$

which we recognize as the product $M = R^\top S R$.

Furthermore, since M is invertible, we have $\operatorname{rank}(M) = \mathfrak{s}(d)\,n$. From the rank inequality on product of matrices, we get

$$\operatorname{rank}(M) \le \min\left(\operatorname{rank}(S), \operatorname{rank}(R)\right) \le \operatorname{rank}(R),$$

meaning that the rank of R is equal to its number of columns $\mathfrak{s}(d)\,n$. The pseudoinverse $R^\dagger$ can therefore be computed as $R^\dagger = (R^\top R)^{-1} R^\top$, and $R^\dagger$ plays the role of a left inverse, i.e., we have $R^\dagger R = \mathbf{I}$.

We thus have $R^\dagger \breve{\mathbf{\Lambda}}_h = R^\dagger R \mathbf{\Lambda}_h = \mathbf{\Lambda}_h$, so (38a) is directly equivalent to (37a). Moreover, since for any positive scalar ξ, $f^\star_{\mathrm{DS}}(\mathbf{x}, \mathbf{y}) = \mathbf{0} \iff f^\star_{\mathrm{DS}}(\mathbf{x}, \xi\mathbf{y}) = \mathbf{0}$, the system is not affected by a multiplication of the left-hand-side of (38b) with the matrix S. Multiplying then both sides of (38b) by $R^\top$, we get

$$R^\top S \breve{\mathbf{\Gamma}}_h = R^\top {R^\dagger}^\top B\,\mathbf{U}_h + R^\top {R^\dagger}^\top \mathbf{k}_{tot}$$

Since $R^\top {R^\dagger}^\top = \left(R^\dagger R\right)^\top = \mathbf{I}$, we retrieve (37b).

Finally, as $\breve{\mathbf{\Lambda}}_h[q] = \overline{\boldsymbol{\lambda}_h}(\breve{x}_q)$ and $\breve{\mathbf{\Gamma}}_h[q] = \overline{\gamma_h}(\breve{x}_q)$, we have (38c) $\iff$ $(\boldsymbol{\lambda}_h(\breve{x}_q); \gamma_h(\breve{x}_q)) \in \mathcal{DP}(\mu, \mathrm{Bi})$, that is, we retrieve the discrete expression of (37c) expressed at quadrature points $\breve{x}_q$. □

This time we have obtained in (38) a system which preserves the symmetry of the new Delassus operator $\breve{W} = {R^\dagger}^\top B\,A^{-1}\,B^\top R^\dagger$. One remaining difficulty stems from the presence of the matrix $R^\dagger$, which in the general case could increase substantially the cost of solving the system.

4.3.5 Considerations on $R^\dagger$

Trapezoidal quadrature rule The first observation is that if the quadrature points $(\breve{x}_q)$ were to coincide with the degrees of freedom (x_i), R would boil down to the identity matrix and the operator $R^\dagger$ would not induce any additional cost. This is actually always the case for a piecewise constant ($\mathbb{P}_0$) approximation, for which both the degrees of freedom and the quadrature points are located at the barycenter of each element.

For higher-order polynomial basis functions, having the $(\breve{x})_q$ coincide with the $(x)_i$ amounts to computing $m(\boldsymbol{\gamma}, \boldsymbol{\tau})$ using a trapezoidal integration rule. Obviously, such an approximation induces a loss of precision – the integral being exact only for functions that are linear between the degrees of freedom. This means that the order of convergence will not increase with that of the basis functions, and using high-order discretization space ($\mathbb{P}_2$ or higher-order polynomials) would be wasteful. However, for piecewise linear ($\mathbb{P}_1$) polynomials, we found such approximation to be acceptable, and used it in practice.

Mixed finite elements In the case of piecewise-polynomial discontinuous basis functions, degrees of freedom are not shared between adjacent elements. When considering such a discretization of the space $T(\Omega)$, the matrix R becomes block-diagonal, and consequently its pseudo-inverse has a similar structure and is easy to compute. The additional cost induced by the presence of the linear operator $R^\dagger$ in Problem (38) is therefore once again negligible.

4.3.6 Final discrete system

For brevity of notation and since there are no more ambiguities, from now on we shall drop the decorations and capitalization of the variables, i.e., we shall consider Problem (38) written as

$$\text{Find } \mathbf{u} \in \mathbb{R}^{\mathfrak{v}},\ \boldsymbol{\lambda}, \boldsymbol{\gamma} \in \mathbb{R}^{\mathfrak{s}(d)\, n_Q}, \begin{cases} A\,\mathbf{u} = B^\top R^\dagger \boldsymbol{\lambda} + \mathbf{l} & \text{(39a)} \\ \boldsymbol{\gamma} = {R^\dagger}^\top B\,\mathbf{u} + {R^\dagger}^\top \mathbf{k} & \text{(39b)} \\ \mathbf{0} = f^\star_{\mathrm{DS}}(\boldsymbol{\lambda}, \boldsymbol{\gamma}), & \text{(39c)} \end{cases}$$

where $f^\star_{\mathrm{DS}}$ is extended from $\mathbb{R}^{\mathfrak{s}(d)}$ to $\mathbb{R}^{n_Q\,\mathfrak{s}(d)}$ by concatenation.

4.4 Solving (39) numerically in the case $\mathrm{Bi} = 0$

In the case when $\mathrm{Bi} = 0$, from Corollary 1 the constraint (39c) boils down to $\mathcal{K}_{\frac{1}{\mu}} \ni \hat{\boldsymbol{\gamma}} \perp \boldsymbol{\lambda} \in \mathcal{K}_\mu$. The resulting problem was extensively studied in the contact mechanics field, see e.g., [Cad09] for a review.

4.4.1 Existence of solutions

A sufficient criterion for the existence of solutions to this problem is given in [Cad09, ACLM11]. In our case, this translates into a compatibility condition on the Dirichlet boundary conditions. More precisely, if the hypothesis $\mathcal{H}(\mu)$ is satisfied,

$$\mathcal{H}(\mu) := \exists \mathbf{u},\ {R^\dagger}^\top (B\mathbf{u} + \mathbf{k}) \in \mathcal{K}_{\frac{1}{\mu}}, \tag{40}$$

then the problem admits a solution, which is unique in $\mathbf{u}$ and $\boldsymbol{\gamma}$ (though not in $\boldsymbol{\lambda}$). Note that for $\mu = 0$, $\mathcal{H}(\mu)$ boils down to the existence of discrete velocity field with positive divergence at each quadrature point. In the absence of non-homogeneous Dirichlet boundary conditions, $\mathbf{k} = 0$ and the solution in $\mathbf{u}$ is guaranteed to exist and to be unique.

4.4.2 Cadoux's algorithm

Several methods have been proposed to decompose Problem (39) as a succession of optimization problems depending on a varying parameter s, see e.g. [HT83, RA05, ACLM11]. We recall in this section the fixed-point algorithm originally presented in [Cad09, ACLM11], which allows us to rewrite our problem as a nested loop of Second-Order Cone Quadratic Problems (**SOCQP**). The advantage of this algorithm over most other approaches is that the successive values of the parameter s depend only on the primal variable $\mathbf{u}$, which is uniquely defined under $\mathcal{H}(\mu)$.

First, let us introduce the reduced (or dual) version of Problem (39), which is derived by eliminating the velocity variable $\mathbf{u}$,

$$\begin{aligned} W\boldsymbol{\lambda} + \mathbf{w} &= \boldsymbol{\gamma} \quad \boldsymbol{\lambda}, \boldsymbol{\gamma} \in \mathbb{R}^{2\mathfrak{s}(d)\, n_Q} \\ f^{\star}_{\mathrm{DS}}(\boldsymbol{\lambda}, \boldsymbol{\gamma}) &= \mathbf{0}, \end{aligned} \tag{41}$$

where $W = R^{\dagger^\top} B A^{-1} B^\top R^\dagger$ and $\mathbf{w} = R^{\dagger^\top}\left(BA^{-1}\mathbf{l} + \mathbf{k}\right)$.

For any value of a parameter $s \in \mathbb{R}_+^{n_Q}$, we define the quadratic function

$$J_s(\boldsymbol{\lambda}) := \frac{1}{2}\boldsymbol{\lambda}^\top W \boldsymbol{\lambda} + \boldsymbol{\lambda}^T(\mathbf{w} + (s;0))$$

and the **SOCQP**

$$\min_{\boldsymbol{\lambda} \in \mathcal{K}_\mu} J_s(\boldsymbol{\lambda}). \tag{42}$$

Corresponding KKT conditions read $\mathcal{K}_{\frac{1}{\mu}} \ni \nabla J_s(\boldsymbol{\lambda}) \perp \boldsymbol{\lambda} \in \mathcal{K}_\mu$, i.e.,

$$\mathcal{K}_{\frac{1}{\mu}} \ni \boldsymbol{\gamma} + (s;0) \perp \boldsymbol{\lambda} \in \mathcal{K}_\mu. \tag{43}$$

Let us introduce the mappings $v : \mathbb{R}_+^{n_Q} \to \mathbb{R}^{\mathfrak{s}(d)\, n_Q}, s \mapsto v(s) := \nabla J_s(\boldsymbol{\lambda}^*(s))$ with $\boldsymbol{\lambda}^*(s)$ a solution to the **SOCQP** (42), and $F : \mathbb{R}_+^{n_Q} \to \mathbb{R}_+^{n_Q}$, $s \mapsto \mu\|v(s)_{\mathrm{T}}\|$. Using a duality argument, Cadoux et al. [Cad09, ACLM11] show that v and therefore F are well-defined.

Solving our problem amounts to finding a fixed-point s^* of F, thus setting $\boldsymbol{\lambda} = \boldsymbol{\lambda}^*(s^*)$. Indeed $s^* = F(s^*) = \mu\|\boldsymbol{\gamma}_{\mathrm{T}} + (s^*;0)_{\mathrm{T}}\| = \mu\|\boldsymbol{\gamma}_{\mathrm{T}}\|$, and therefore the KKT conditions (43) yield

$$\mathcal{K}_{\frac{1}{\mu}} \ni \boldsymbol{\gamma} + (\mu\|\boldsymbol{\gamma}_{\mathrm{T}}\|;0) \perp \boldsymbol{\lambda} \in \mathcal{K}_\mu.$$

We identify the bipotential $\hat{\boldsymbol{\gamma}} := \boldsymbol{\gamma} + (\mu\|\boldsymbol{\gamma}_{\mathrm{T}}\|;0)$ and get $f^{\star}_{\mathrm{DS}}(\boldsymbol{\lambda}, \boldsymbol{\gamma}) = \mathbf{0}$.

Data: $\boldsymbol{\lambda}$ initial guess
Data: $\varepsilon > 0$ tolerance
Result: $(\boldsymbol{\lambda};\boldsymbol{\gamma})$ satisfying (41)
Loop
  $\boldsymbol{\gamma} \leftarrow W\boldsymbol{\lambda} + \mathbf{w}$;
  break if $|f_{\mathrm{AC}}(\boldsymbol{\lambda}, \boldsymbol{\gamma})| < \varepsilon$;
  $s \leftarrow \mu\|\boldsymbol{\gamma}\|$;
  $\boldsymbol{\lambda} \leftarrow$ solution of **SOCQP** (42) at s ;
end

Algorithm 1: Fixed-point algorithm with Alart-Curnier stopping criterion

It is not known whether F is a contraction. However, we observe very good convergence in pratice of the fixed-point algorithm 1. More complex rules for iterating on s have been investigated in [Cad09] but have not been found to perform significantly better.

4.4.3 Second Order Cone Programing

The easiest way to tackle the **SOCQP** (42) is to leverage the efficiency of out-of-the-box interior-points solvers for Second Order Cone Programs (**SOCP**), of which it is a subclass.

The first step consists in removing the quadratic part of the objective function by introducing a variable $t \in \mathbb{R}$ subject to the constraint $t \geq \frac{1}{2}\boldsymbol{\lambda}^\top W \boldsymbol{\lambda}$. The new objective is $\hat{J}_s(t, \boldsymbol{\lambda}) = t + \boldsymbol{\lambda}^T(\mathbf{w} + (s; 0))$.

Given a square root L of A, we have $A = LL^\top$ and $W = (L^{-1}B^T R^\dagger)^\top L^{-1} B^\top R^\dagger$. With an auxiliary variable $\mathbf{y} \in \mathbb{R}^{\mathfrak{v}}$ that satisfies $L\mathbf{y} = B^\top R^\dagger \boldsymbol{\lambda}$, the constraint on t now reads $2t \geq \mathbf{y}^\top \mathbf{y}$ and may also be written as a rotated cone constraint $(1, t, \mathbf{y}) \in \mathcal{RK}$.

We obtain the **SOCP**

$$\begin{aligned} \min_{t \in R, \boldsymbol{\lambda} \in \mathbb{R}^{\mathfrak{s}(d)\, n_Q}} \quad & t + \boldsymbol{\lambda}^\top (\mathbf{w} + (s; 0)) \\ R\mathbf{z} &= \boldsymbol{\lambda} \\ L\mathbf{y} &= B^\top \mathbf{z} \\ \boldsymbol{\lambda} &\in \mathcal{K}_\mu^{n_Q} \\ (1, t, \mathbf{y}) &\in \mathcal{K}_1. \end{aligned}$$

4.4.4 Projected Gradient

The interior-point approach has some drawbacks: arguably, the reliance on a complex external code, but most importantly, the inability of interior-point solvers to be warm-started. As our outer fixed-point loop converges, the quality of our initial guess increases and we would like the **SOCQP** solver to take advantage of this.

Another natural way to solve the **SOCQP** is to use a Projected Gradient (**PG**) algorithm. In its simplest form, it reads

Data: $\boldsymbol{\lambda}$ initial guess
Data: Step length $\xi > 0$
Result: $\boldsymbol{\lambda}$ solution of **SOCQP** (42)
Loop
  $\mathbf{y} \leftarrow W\boldsymbol{\lambda} + \mathbf{w} + (s; 0)$;
  $\mathbf{x} \leftarrow \Pi_{\mathcal{K}_\mu}(\boldsymbol{\lambda} - \xi \mathbf{y})$;
  break if $|\mathbf{x} - \boldsymbol{\lambda}| < \varepsilon$;
  $\boldsymbol{\lambda} \leftarrow \mathbf{x}$
end

Algorithm 2: Canonical Projected Gradient algorithm.

Since Algorithm (2) can converge quite slowly in practice, several works have focused on finding ways to improve its speed, among which we note

- Performing a line-search of the step size ξ;
- The Accelerated Gradient method from Nesterov [Nes83], adapted to **SOCQP** in [Hey13];
- The Spectral Gradient method from Barzilai et al. [BB88], adapted to **SOCQP** in [Tas13].

Using such techniques, we found the **PG** method to be competitive with interior-points solvers on our problem, especially as the outer fixed-point loop converges and the quality of the intial guess increases. Numerical details are provided in Section 6.4.

4.4.5 Primal algorithm

In some situations, one may only be interested in the primal variable $\mathbf{u}$, and do not need the value of the dual variable $\boldsymbol{\lambda}$. In this case, following [Cad09] again, we can implement the fixed-point algorithm directly on the primal formulation, and avoid the need for some auxiliary variables.

The insight is that the **SOCQP** (42) admits a dual problem, namely

$$\min_{R^{\dagger\top}(B\mathbf{u}+\mathbf{k}+(s;0))\in\mathcal{K}_{\frac{1}{\mu}}} \frac{1}{2}\mathbf{u}^\top A\mathbf{u} - \mathbf{u}^\top\mathbf{l}. \tag{44}$$

Data: $\mathbf{u}$ initial guess
Data: $\varepsilon > 0$ tolerance
Result: $\mathbf{u}$ satisfying (39)
Loop
  $\boldsymbol{\gamma} \leftarrow R^{\dagger\top}(B\mathbf{u}+\mathbf{k})$;
  $s \leftarrow \mu\|\boldsymbol{\gamma}\|$;
  $\mathbf{u} \leftarrow$ solution of **SOCQP** (44) at s ;
  break if successive iterates close enough;
end

Algorithm 3: Primal version of the fixed-point algorithm

Algorithm 1 can then be trivially adapted to use the primal minimization problem, as in Algorithm 3. Due the to complex nature of the constraint, the **SOCQP** (44) is not suited for a Projected-Gradient algorithm, however it can be just as easily put under a **SOCP** form.

$$\begin{aligned}
\min_{t\in R,\mathbf{u}\in\mathbb{R}^\upsilon}\ & t - \mathbf{u}^\top\mathbf{l} \\
R^\top\mathbf{z} &= B\,\mathbf{u} + \mathbf{k} + (s;0) \\
\mathbf{y} &= L^\top\mathbf{u} \\
\mathbf{z} &\in \mathcal{K}_{\frac{1}{\mu}}^{n_Q} \\
(1,t,\mathbf{y}) &\in \mathcal{K}_1
\end{aligned}$$

Remark 2. *Unlike the dual version, this algorithm does not generalize to the case* $\mathrm{Bi} > 0$.

4.5 Solving (39) numerically in the case $\mathrm{Bi} > 0$

The case $\mathrm{Bi} > 0$, where the **SOC** $\mathcal{K}_\mu$ is replaced with the truncated one $\mathcal{K}_{\mu,\mathrm{Bi}}$, has not been as extensively studied in the literature. While a rigorous proof for establishing an existence criterion is beyond the scope of this paper, in this section we will justify that

- A simple modification to the Projected-Gradient algorithm is sufficient to solve our problem;
- Every step of the algorithm can be computed, or in other terms, every optimization problem that appears in the algorithm admits a solution.

4.5.1 Modified PG algorithm

We modify Algorithm 2 so that $\boldsymbol{\lambda} - \xi\mathbf{y}$ is projected onto $\mathcal{K}_{\mu,\mathrm{Bi}}$ instead of $\mathcal{K}_\mu$. When the algorithm converges, we have $\Pi_{\mathcal{K}_{\mu,\mathrm{Bi}}}(\boldsymbol{\lambda} - \xi\nabla J_s(\boldsymbol{\lambda})) = 0$, which means that $\boldsymbol{\lambda}$ is a solution of the minimization problem

$$\min_{\boldsymbol{\lambda}\in\mathcal{K}_{\mu,\mathrm{Bi}}} J_s(\boldsymbol{\lambda}). \tag{45}$$

Now, suppose that $s^* \in \mathbb{R}_+^{nQ}$ is a fixed-point of the Cadoux algorithm with the new applications defined as $v_{\mathrm{Bi}} : \mathbb{R}_+^{nQ} \to \mathbb{R}^{\mathfrak{s}(d)\,nQ}, s \mapsto v_{\mathrm{Bi}}(s) \coloneqq \nabla J_s(\boldsymbol{\lambda}^*(s))$ with $\boldsymbol{\lambda}^*(s)$ a solution to (45), and $F_{\mathrm{Bi}} : \mathbb{R}_+^{nQ} \to \mathbb{R}_+^{nQ}$, $s \mapsto \mu \| v_{\mathrm{Bi}}(s)_{\mathrm{T}} \|$.

Then once again we have $v_{\mathrm{Bi}}(s^*) = \boldsymbol{\gamma} + (\mu \|\boldsymbol{\gamma}_{\mathrm{T}}\|; 0) = \hat{\boldsymbol{\gamma}}$, and therefore $\Pi_{\mathcal{K}_{\mu,\mathrm{Bi}}}(\boldsymbol{\lambda} - \xi\hat{\boldsymbol{\gamma}}) = 0$ which exactly amounts to $f^{\star}_{\mathrm{DS}}(\boldsymbol{\lambda}, \boldsymbol{\gamma}) = \mathbf{0}$.

4.5.2 Existence of a solution to (45)

In this paragraph, we justify that if the criterion (40) is satisfied, then $\forall s \in \mathbb{R}_+^{nQ}$, the minization problem (45) admits a solution. Therefore we can compute every iteration of the Cadoux fixed-point algorithm.

Let us suppose that the hypothesis $\mathcal{H}(\mu)$ defined in Eq (40) is satisfied. This implies $R^\dagger \mathbf{k} \in \operatorname{Im} H + \mathcal{K}_{\frac{1}{\mu}}$, with H defined as $H \coloneqq R^\dagger B$. Therefore $\mathbf{w} = R^\dagger \mathbf{k} + H A^{-1} \mathbf{l} \in \operatorname{Im} H + \mathcal{K}_{\frac{1}{\mu}}$, or in other words, $\mathbf{w}$ can be decomposed as $\mathbf{w} \coloneqq \mathbf{w}_H + \mathbf{w}_K$, with $\mathbf{w}_H \in \operatorname{Im} H$ and $\mathbf{w}_K \in \mathcal{K}_{\frac{1}{\mu}}$.

Now, we shall express J_s as the sum of three convex quadratic functions and show that each of them is bounded from below on the feasible set $\mathcal{K}_{\mu,\mathrm{Bi}}$.

Proof. Indeed, $J_s = a + b + c$, with

$$\begin{aligned} a(\boldsymbol{\lambda}) &= \frac{1}{2} \boldsymbol{\lambda} W \boldsymbol{\lambda} + \boldsymbol{\lambda}^\top \mathbf{w}_H \\ b(\boldsymbol{\lambda}) &= \boldsymbol{\lambda}^\top \mathbf{w}_K \\ c(\boldsymbol{\lambda}) &= \boldsymbol{\lambda}^\top (s; 0) \end{aligned}$$

Since $\operatorname{Im} W = \operatorname{Im} H$, $\exists \mathbf{x}$ s.t. $W\mathbf{x} = -\mathbf{w}_H$ and as W is positive semi-definite $a(\mathbf{x})$ is a minimum of a on $\mathbb{R}^{nQ} \times \mathbb{R}^{\mathfrak{s}(d)\,nQ}$. The restriction of a to $\mathcal{K}_{\mu,\mathrm{Bi}}$ is therefore bounded from below. Moreover, since $s \in \mathbb{R}_+^{nQ}$, $\forall \boldsymbol{\lambda} \in \mathcal{K}_{\mu,\mathrm{Bi}}$ $c(\boldsymbol{\lambda}) \geq 0$, and the minimum is attained at $c(0) = 0$.

It is now sufficient to show that b admits a minimum on $\mathcal{K}_{\mu,\mathrm{Bi}}$, which can be rewritten as

$$\exists \mathbf{x} \in \mathcal{K}_{\mu,\mathrm{Bi}}, -\nabla b(\mathbf{x}) \in \mathcal{N}_{\mathcal{K}_{\mu,\mathrm{Bi}}}(\mathbf{x})$$

where $\mathcal{N}_C(\mathbf{x})$ denotes the normal cone to the convex set C at $\mathbf{x}$. Since $\nabla b(\mathbf{x}) = \mathbf{w}_K$, this is equivalent to

$$\mathbf{w}_K \in \bigcup_{\mathbf{x} \in \mathcal{K}_{\mu,\mathrm{Bi}}} -\mathcal{N}_{\mathcal{K}_{\mu,\mathrm{Bi}}}(\mathbf{x}) = \mathcal{K}_{\frac{1}{\mu}}.$$

□

We can therefore write

$$\forall \mathbf{x} \in \mathcal{K}_\mu, J_s(\mathbf{x}) \geq \inf_{\mathcal{K}_{\mu,\mathrm{Bi}}} a + \min_{\mathcal{K}_{\mu,\mathrm{Bi}}} b + \min_{\mathcal{K}_{\mu,\mathrm{Bi}}} c,$$

which means that J_s is bounded from below on the feasible set. The attainability of its minimum on $\mathcal{K}_{\mu,\mathrm{Bi}}$ follows from the extension of the Frank-Wolfe theorem to Convex Quadratically Constrained Quadratic Programming [LZ99].

5 Inertial flows

5.1 Continuous equations

We now add an inertial term to our momentum conservation equations. We only consider purely compressive scenarios, so the density ρ is assumed to remain constant.

$$\rho\left(\frac{\partial \mathbf{u}}{\partial t} + (\mathbf{u}\cdot\nabla)\mathbf{u}\right) - \nabla\cdot\left[2\nu\,\mathrm{D}^b(\mathbf{u}) + \boldsymbol{\tau}\right] + \nabla p = \rho\mathbf{g}$$

With the dimensionless time $\tilde{t}$ defined such that $t = \frac{L}{U}\tilde{t} = \sqrt{\frac{L}{g}}\tilde{t}$, the full system reads

$$\begin{aligned}
\tfrac{\partial}{\partial \tilde{t}}\tilde{\mathbf{u}} + (\tilde{\mathbf{u}}\cdot\nabla)\tilde{\mathbf{u}} - \tilde{\nabla}\cdot\left[\tfrac{2}{\mathrm{Re}}\widetilde{\mathrm{D}^b}(\tilde{\mathbf{u}}) - \tilde{\boldsymbol{\lambda}}\right] &= \mathbf{e}_g && \text{on } \Omega\\
\tilde{\mathbf{u}} &= \tilde{\mathbf{u}}_D && \text{on } B_D\\
\widetilde{\mathrm{D}^b}(\tilde{\mathbf{u}})\,\mathbf{n}_\Omega &= 0 && \text{on } B_N\\
\left(\tilde{\boldsymbol{\lambda}}; \tilde{\mathrm{D}}(\tilde{\mathbf{u}})\right) &\in \mathcal{DP}(\mu, \mathrm{Bi}) && \text{on } \Omega
\end{aligned}$$

As in the previous section, we will drop the tildes from now on.

5.2 Discretization

The notation $\frac{\partial \mathbf{u}}{\partial t}$ in previous paragraphs is misused. Indeed, due to the nonsmoothness of the rheology $\mathcal{DP}(\mu, \mathrm{Bi})$, $\mathbf{u}(t)$ may not be time-differentiable at every instant. Rigorously, it should be written as a *measure differential inclusion*. Fortunately, the so-called Moreau sweeping process [Mor99] ensures that a standard timestepping (or catch-up) algorithm will still converge as expected towards the continuous solution as the timestep Δ_t is refined.

While directly discretizing directly the transport term $(\mathbf{u}\cdot\nabla)\mathbf{u}$ would be tempting, this ultimately leads to the addition of a non-symmetric form to our equations, which breaks our resolution framework.

Instead, we use a more classical first-order characteristics scheme. The total derivative is approximated as

$$\frac{\partial \mathbf{u}}{\partial t} + (\mathbf{u}\cdot\nabla)\mathbf{u} \sim \frac{\mathbf{u}^{k+1} - \mathbf{u}^k \circ X^k}{\Delta_t}$$

where $X^k(x) \coloneqq x - \Delta_t \mathbf{u}^k(x)$

The variational formulation is obtained by taking the forms defined in paragraph 4.2 and adding the following terms to l and a,

$$\begin{aligned}
a(\mathbf{u},\mathbf{v}) &\coloneqq a_{(4.2)}(\mathbf{u},\mathbf{v}) + \frac{1}{\Delta_t}\int_\Omega \mathbf{u}\cdot\mathbf{v}\\
l(\mathbf{v}) &\coloneqq l_{(4.2)}(\mathbf{v}) + \frac{1}{\Delta_t}\int_\Omega \left(\mathbf{u}^k \circ X^k\right)\cdot\mathbf{v}.
\end{aligned}$$

Solving for each timestep in the dynamics setting is therefore equivalent to solving the problem defined in Section 4.

Remark 3. *Note that the time-stepping scheme ensures a positive-definite form a even when* $\frac{1}{\mathrm{Re}} = 0$. *This allows us to simulate purely plastic flows, instead of being restricted to viscoplastic ones as in Section 4.*

6 Results

All the finite element simulations presented in this section were performed using the open-source library Rheolef [Sar12]. When solving the **SOCP** formulation of the inner problem, we used the commercial package MOSEK [ART03]. The benchmarks were run on a standard quad-core Intel(R) Xeon W3520 machine with 8GB memory.

6.1 Model problems

In this section, we validate our solver on simple problems for which we can derive analytic solutions.

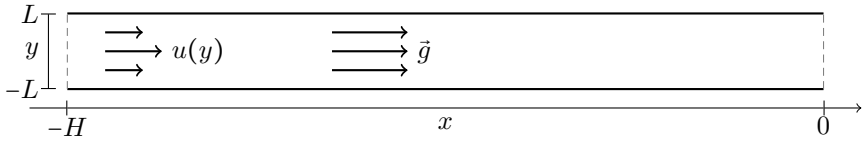

Figure 3: 2D channel for the Bingham Poiseuille flow

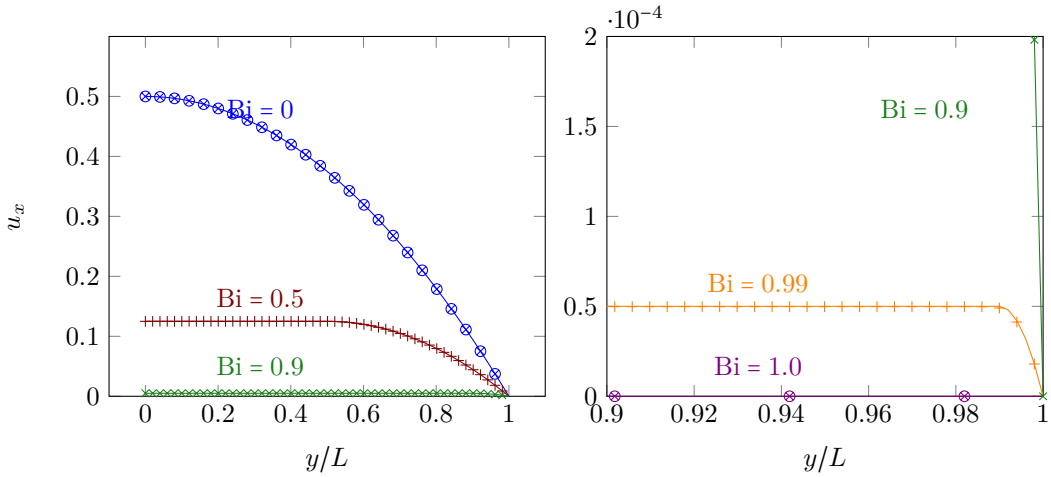

Figure 4: Comparison of the steady velocity profiles $u_x(-H/2, y)$ between our numerical model using a $\mathbb{P}_2 - \mathbb{P}_{1d}$ approximation (marks), and the analytic Bingham Poiseuille flow (lines). Plots for high values of Bi (right) are zoomed in compared to plots for lower Bi values (left).

6.1.1 Bingham Poiseuille flow

We consider a Bingham Poiseuille flow as illustrated in Figure 3, with the following boundary conditions,

$$\mathbf{u}(x, -L) = \mathbf{u}(x, L) = 0 \quad \forall x \in [-H, 0] \qquad \text{No-slip on walls}$$
$$\mathbf{u}(-H, y) = u_x(-H, y)\mathbf{e}_x \quad \forall y \in [-L, L] \qquad \text{Upstream velocity along axis}$$
$$\mathbf{u}(0, y) = u_x(0, y)\mathbf{e}_x \quad \forall y \in [-L, L] \qquad \text{Downstream velocity along axis.}$$

Figure 4 shows velocity profiles for different values of Bi, for both the analytic solution and our model using a $\mathbb{P}_4 - \mathbb{P}_{1d}$ approximation. Using a nonsmooth solver allows us to recover the correct profile even for high values of Bi without any parameter tuning.

6.1.2 Convergence of spatial discretization

We study how the error between our method and the analytic solution decreases as we uniformly refine a mesh with initial characteristic edge length h_0. Results for Bi = 0.5 and Bi = 0.9 are shown in Figure 5, the norm $\|\cdot\|_\infty$ and various FEM approximation orders. Convergence was observed for all approximation orders, and we found that $\mathbb{P}_2 - \mathbb{P}_1$ and $\mathbb{P}_2 - \mathbb{P}_{1d}$ achieved a good ratio of convergence speed versus computational cost. Conversely, the higher-order approximation $\mathbb{P}_3 - \mathbb{P}_{2d}$ performed relatively poorly on the finer meshes, which we interpret as being the result of numerically more complex quadrature rules. $\mathbb{P}_4$–$\mathbb{P}_{1d}$, with high-order velocities but low-order stresses, yielded consistently the best results, at the cost of a very large A matrix.

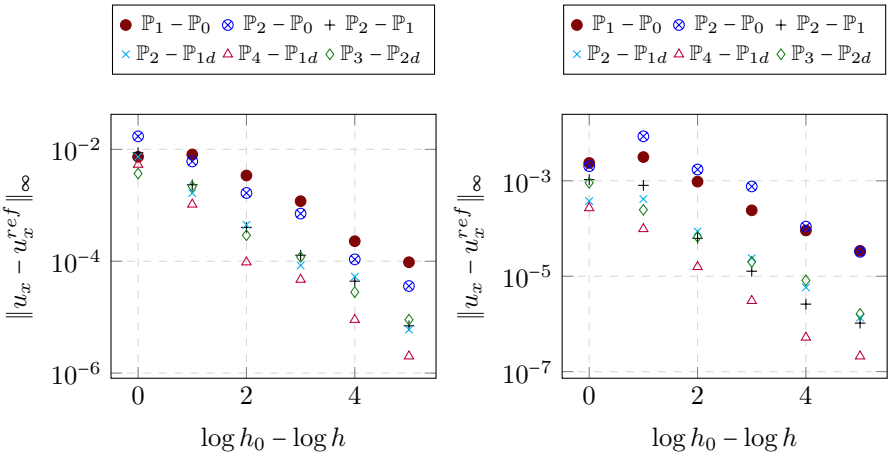

Figure 5: Convergence plots for various FEM approximation orders, for $Bi = 0.5$ (left) and $Bi = 0.9$ (right). u_x^{ref} denotes the analytical solution.

6.1.3 Bagnold profiles

We consider the flow of a granular layer of height $H = 1$ on a rough infinite inclined plane with angle α, as described in [LSP11] and illustrated in Figure 6. We assume the flow to be slow enough to neglect inertial terms.

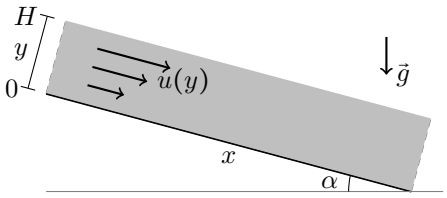

Figure 6: Flow on an infinite inclined plane

The conservation of momentum on the longitudinal x-axis and perpendicular y-axis reads

$$\frac{\partial}{\partial y}\left(\eta\frac{\partial u}{\partial y} + \tau_{xy}\right) = -\sin\alpha$$
$$\frac{\partial p}{\partial y} = -\cos\alpha.$$

Integrating the second equation with the condition that the pressure should be zero at the top of the granular layer, i.e., $p(H) = 0$, gives $p = (1 - y)\cos\alpha$.

We consider the case of an avalanching flow with $\frac{\partial u}{\partial y} > 0$ for $y < 1$. This means that the friction is saturated, therefore $\tau_{xy} = \mu(1 - y)\cos(\alpha)$. We get

$$\frac{\partial}{\partial y}\eta\frac{\partial u}{\partial y} = -\sin\alpha + \mu\cos\alpha.$$

A Neumann boundary condition at the interface $\frac{\partial u}{\partial y}(1) = 0$ imposes $\frac{\partial}{\partial y}\eta\frac{\partial u}{\partial y} < 0$, which means $\mu < \tan\alpha$.

For spatially constant (Newtonian) η and μ, we get $\frac{\partial u}{\partial y} = \frac{1-y}{\eta}\sin\alpha - (\mu\cos\alpha)$, and $u(y)$ is quadratic. In order to retrieve the typical $\frac{3}{2}$ power of the Bagnold profile, we can instead choose $\eta(y) := |\mathrm{D}(u)| = \frac{1}{2}\frac{\partial u}{\partial y}$, which gives the analytic expressions

$$\frac{\partial u}{\partial y} = \sqrt{2\sin\alpha - (\mu\cos\alpha)}\,(1-y)^{\frac{1}{2}}$$
$$u(y) = \frac{2}{3}\sqrt{2\sin\alpha - (\mu\cos\alpha)}\left(1-(1-y)^{\frac{3}{2}}\right).$$

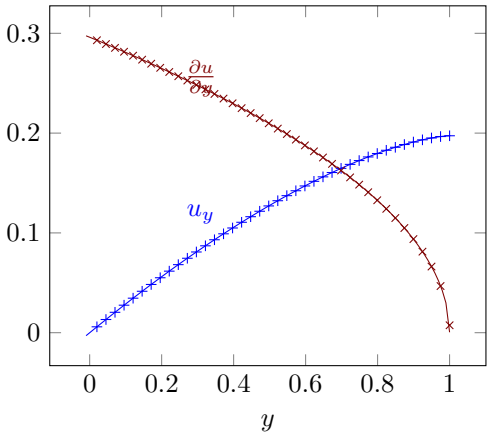

Figure 7: Comparison between our numerical solution (marks) and the analytic one (lines), for the velocity and shear-rate profiles of a Bagnold avalanche flow with $\mu = 0.5$ and $\alpha = \tan^{-1}(1.1\mu)$.

We simulated this model on a square patch using the algorithm presented in Section 4. The value of $\boldsymbol{\sigma}_{ext}$ on the upstream and downstream boundaries was computed using the analytic solution. In order to handle the non-constant η, we used a fixed-point algorithm which happened to converge very fast in practice – a dozen or so of iterations.

Numerical and analytic profiles are compared in Figure 7. Once again, we observe a very good agreement between our model and the analytic solution.

6.2 Discharge of a silo

In this section we attempt to simulate a problem that has been widely studied both experimentally and numerically: the discharge of a granular silo.

6.2.1 Beverloo scaling

One of the most widely accepted macroscopic feature of the granular flow in a silo is the so-called Berveloo scaling [BLvdV61], stating that the discharge rate Q depends on the diameter of the outlet to the power $d - \frac{1}{2}$,

$$Q = C\sqrt{g}\,(L - kd_p)^{d-\frac{1}{2}},$$

where d_p is the diameter of a grain, and C and k are dimensionless constants depending on the silo geometry and granular properties. The number k typically lies within the range $1 < k < 3$.

The Beverloo phenomenon is particularly relevant for us as it has been shown that such a scaling cannot be recovered for Newtonian flows [SLP12], nor for flows with a yield stress

that does not depend on the pressure. The physical justification of the scaling involves inertia [MJA+07], so it is hopeless to attempt to retrieve it solely with the formulation of Section 4. For this problem, we therefore use the dynamic setting presented in Section 5.

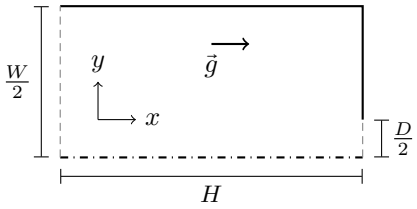

Figure 8: Geometry of a half-silo of heigth H, width W and aperture size D

We simulated the 2D silo shown in Figure 8, with $W = H = 8L$ and an aperture size D. We made the ratio $\tilde{D} := \frac{D}{L}$ vary from $\frac{1}{2}$ to 2, and studied the change in the dimensionless discharge rate $\tilde{Q}$ defined such that $Q := \sqrt{g}L^{\frac{3}{2}}\tilde{Q}$.

Plots for different rheologies, with the corresponding Beverloo fits when one was found, are shown in Figure 9. Beverloo law coefficients for $\mu = 0.6$, for which the fit was always acceptable except for Re = 1, are given in Table 1. Coefficients for $\mu = 0.4$ are also given when the fit was deemed of sufficient quality. We remark that decreasing Re, increasing μ or increasing Bi all contribute to a consequent increase of k. μ and Bi have also a positive impact on C, while Re has only a small influence on this parameter.

		Re = 100		Re = 1000	Re = 10
		Bi = 0	Bi = 0.1	Bi = 0	
$\mu = 0.3$	C	1.70	1.44	1.77	2.00
	k	0	0.96	0	3.34
$\mu = 0.4$	C	1.54	1.52	1.54	1.48
	k	0.87	2.49	0.38	3.07
$\mu = 0.5$	C	1.35	1.43	1.35	1.33
	k	0.83	3.2	0.22	3.56

Table 1: Beverloo law coefficents obtained for $\mu = 0.6$ and $\mu = 0.4$, for different Bi and Re values. The values for k are given assuming $L = 11.2d_p$.

6.2.2 Extension to the $\mu(I)$ rheology

The $\mu(I)$ rheology is classically integrated into dynamics solvers by explicitly evaluating the value of the equivalent viscosity η_{tot} at each timestep [LSP11].

In our case, we only have to explicitely evaluate the friction coefficient $\mu(I)$ instead of η_{tot}. Since $\mu(I)$ can only take values in $[\mu_s, \mu_s + \Delta_\mu]$ whereas η_{tot} takes values in $\mathbb{R}^+$, our approach has a few benefits:

- We do not have to clamp the value of η_{tot}, and can have fully rigid zones where the shear rate is strictly zero (which means an infinite η_{tot})
- The loss of stability of the time-integration scheme due to this explicit term is much less dramatic

While the simulation frameworks are quite different — we do not take into account the air phase and use a non-zero (Re = 100) Newtonian viscosity, we nevertheless attempted to

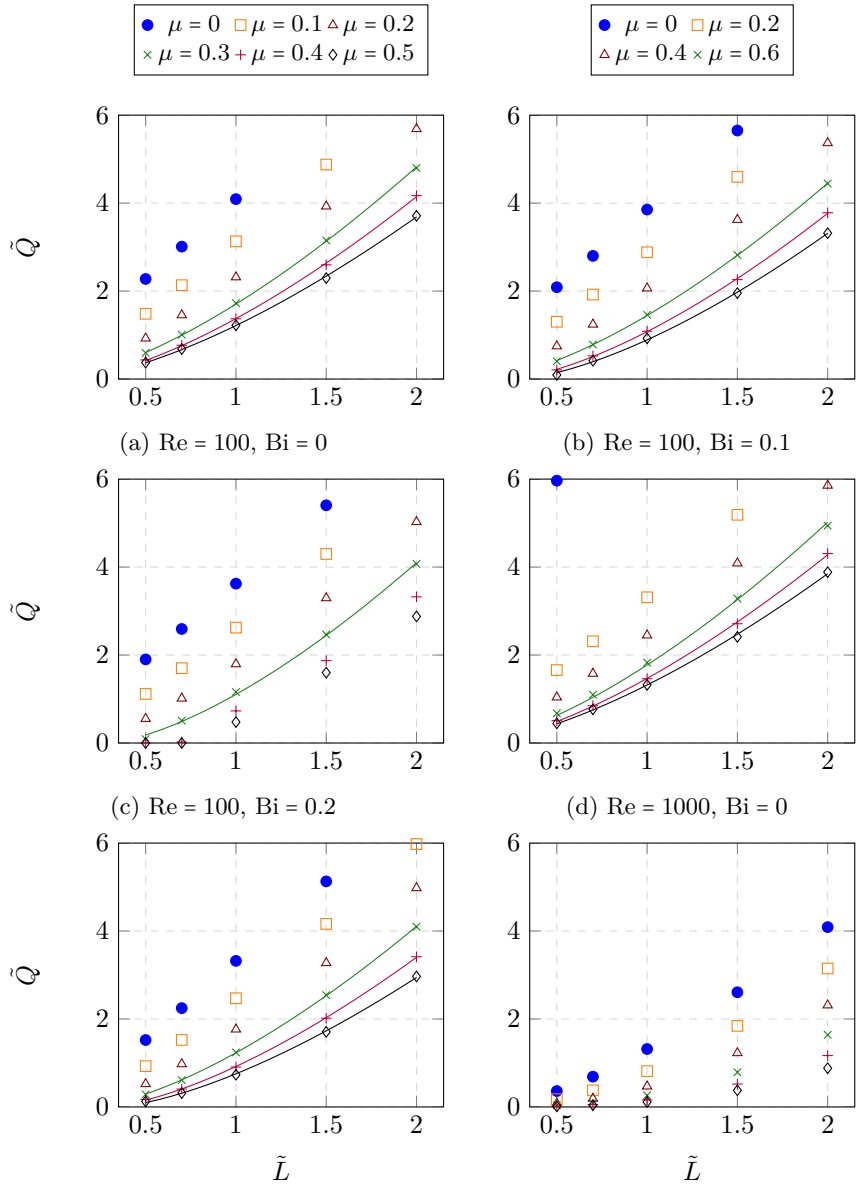

(a) Re = 100, Bi = 0

(b) Re = 100, Bi = 0.1

(c) Re = 100, Bi = 0.2

(d) Re = 1000, Bi = 0

(e) Re = 10, Bi = 0

(f) Re = 1, Bi = 0

Figure 9: Dimensionless discharge rate $\tilde{Q}$ versus silo outlet diameter $\tilde{L}$ for and different rheologies. When μ is small, we cannot get a reasonable fit; in the case of the Newtonian flow, the discharge rate is closer to a linear law. Bi mainly influences the k parameter of the law but does suffices to obtain a fit. Large values of Re tend to linearize the discharge rate for small μ, smaller values make it quadratic.

recreate a simulation from [SLP14, Fig 4], using the same physical parameters ($D = 11.2d_p$, $I_0 = 0.4$, $\mu = 0.32$, $\Delta_\mu = 0.28$).

The results are shown in Figure 10 ; the match on the C coefficient of the Beverloo law is surprisingly good (both methods give $C = 1.48$), however we retrieve a coefficient k that is significantly smaller (0.52 vs 0.73). Velocity profiles along the vertical and horizontal sections described in [SLP14] are also presented in Figure 10.

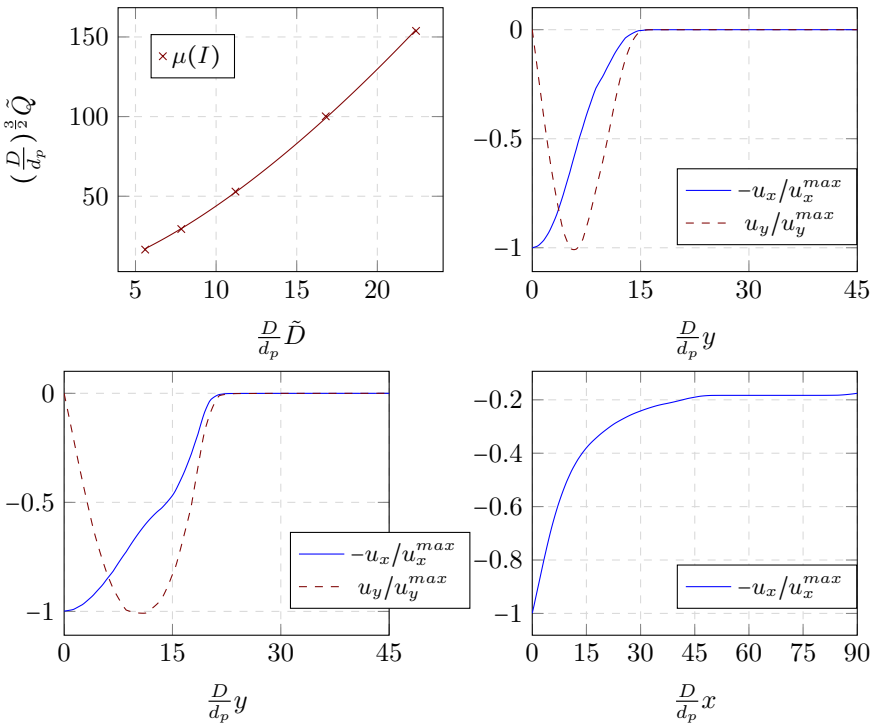

Figure 10: Top-left: Discharge rate as a function of the outlet size for the $\mu(I)$ rheology. The coefficients of the Beverloo fit are, using the dimensionless unit of [SLP14], $C = 1.47$ and $k = 0.063$. Top-right and bottom: Horizontal and vertical velocity profiles for $\tilde{D} = 1$ along section $S1$, $S2$ and $H1$, as defined in [SLP14, Fig. 6]

6.2.3 Visualization of velocity and stress fields

We extend the silo mesh slightly below the outlet and plot the steady-state velocity and stress fields for flows with and without inertia. Results are shown in Figures 11, 12 and 13.

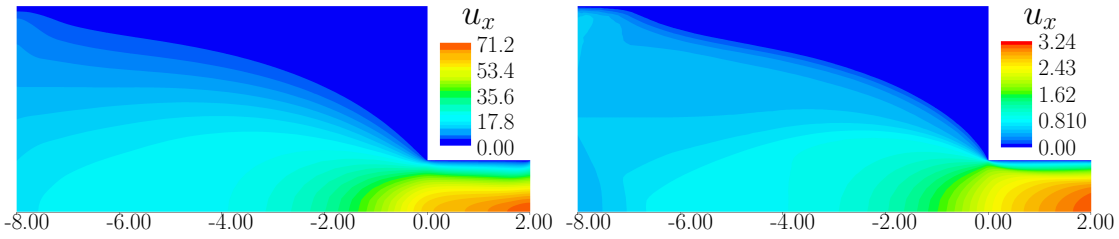

(a) Without inertia (b) With inertia

Figure 11: Axial velocity u_x for simulations with and without inertia for Re = 100, μ = 0.3 and Bi = 0.

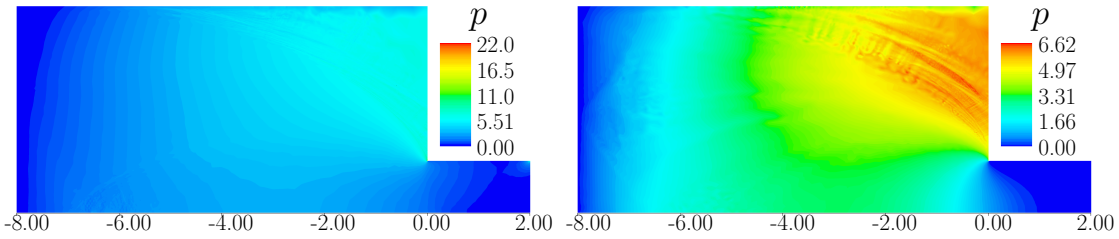

(a) Without inertia (b) With inertia

Figure 12: Pressure fields for simulations with and without inertia for Re = 100, μ = 0.3 and Bi = 0. In the creeping flow case, there exist a very high pressure point on the boundary of the outlet. In the inertial case, the high-pressure zone on the bottom of the silo starts at some distance from the outlet and is much more widely spread.

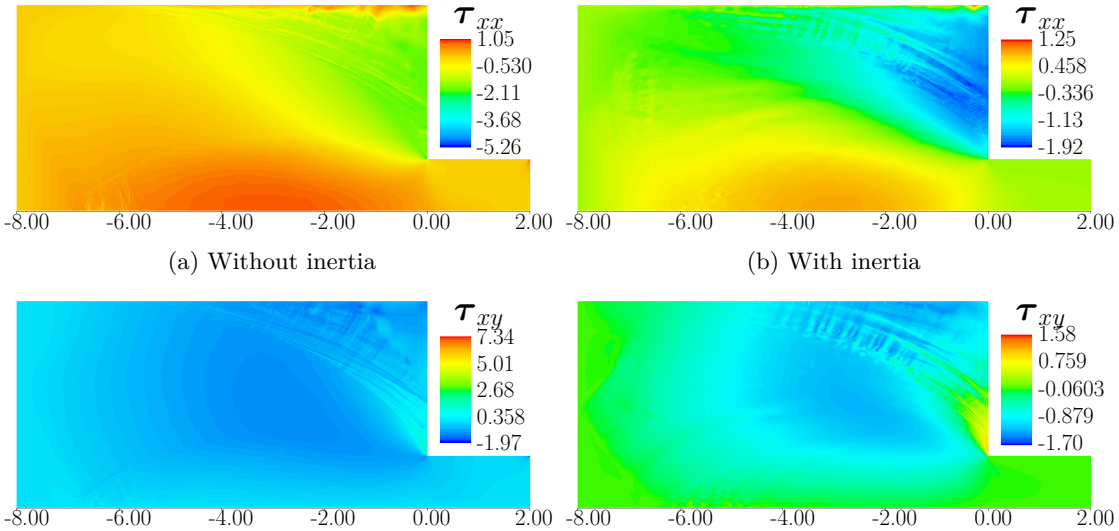

(a) Without inertia (b) With inertia

(c) Without inertia (d) With inertia

Figure 13: Normal (top) and tangential (bottom) components of the deviatoric stress tensor $\boldsymbol{\tau}$ for simulations with and without inertia for Re = 100, μ = 0.3 and Bi = 0.

6.3 Flow around a cylinder

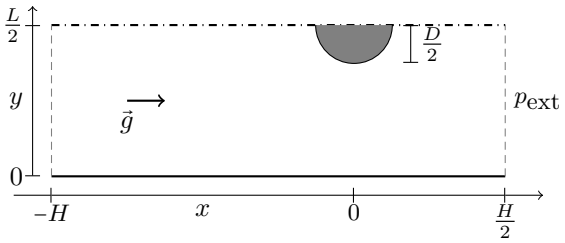

Figure 14: Flow around a cylinder of diameter D in 2D channel of width L. The speed of the flow can be adjusted by varying the external pressure at the downstream boundary p_{ext}.

In this section, we study a gravity induced flow in a 2D channel of width L around a cylinder of diameter D, as shown in Figure 14. We use no-slip boundary conditions for the velocity on the sides of the channel and on the cylinder, and homogeneous Neumann conditions at the upstream and downstream boundaries.

6.3.1 Drag

We attempt to reproduce the experimental setting presented in [CZW03]. Using a regularization of the $\mu(I)$ rheology, Chauchat and Médale [CM14] performed simulations that showed a good qualitative agreement with the experimental results. However, their approach suffered from two drawbacks

- The regularization induces a creeping flow even when none should occur
- The $\nabla \cdot \mathbf{u} = 0$ condition leads to negative pressures behind the obstacle. This is outside the domain of validity of the $\mu(I)$ rheology.

Our method also suffer from approximations; we assume a constant volume fraction of grains, even if this should clearly not be the case behind the obstacle. As the flow is slow, we also neglect its inertia. We use a constant friction coefficient, $\mu = 0.5$, and set $\text{Re} = 100$ and $\text{Bi} = 0$. We vary the average upstream velocity U_∞ by setting different values for the external pressure p_{ext} at the downstream interface; the lower this pressure, the faster the grains will flow. This emulates the varying outlet size in [CZW03]. We set no external pressure at the upstream boundary.

The grains exerce a longitudinal drag force on the cylinder O that can be computed as $F_D := \int_{\partial O} \boldsymbol{\lambda} \mathbf{n}_O . \mathbf{e}_x$. The Froude number is defined from the adimensional average upstream velocity U_∞ and the length ratio $\tilde{D} := \frac{D}{L}$ as $\text{Fr} := \frac{U_\infty}{\sqrt{\tilde{D}}}$.

The dimensionless equivalent drag coefficient C_D is then deduced as

$$C_D := \frac{F_D}{\frac{1}{2} U_\infty^2 \tilde{D}}$$

Figure 15 shows on a logarithmic scale the evolution of the drag coefficient C_D with the Froude number (left) or average velocity (right), for different cylinder diameters. We retrieve the linear profiles observed in [CZW03, CM14]. The fact that the data points for the different diameters become aligned on the right plot means that the slope of $\frac{F_D}{\frac{1}{2}\tilde{D}}$ is independent of $\tilde{D}$; the drag force depends linearly on the diameter of the obstacle.

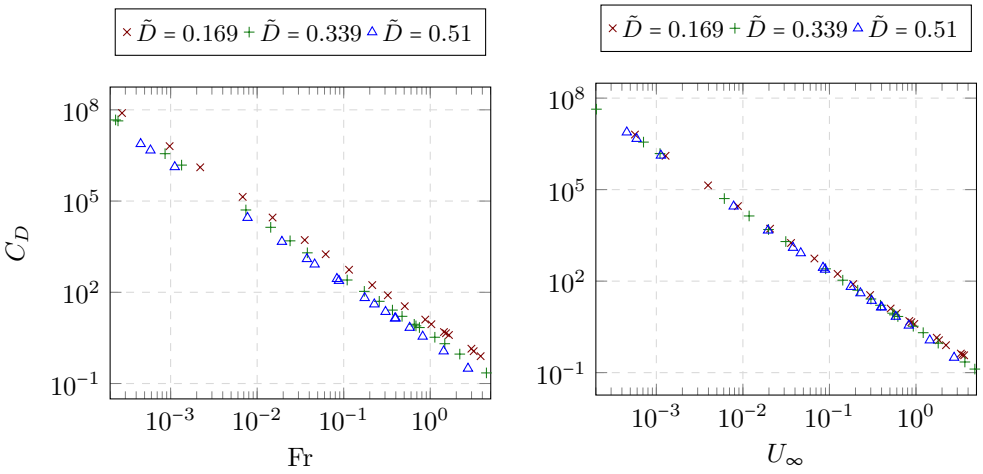

Figure 15: Drag coefficient C_D versus Froude number Fr (left) and upstream velocity U_∞ (right) for the granular flow around a cylinder

6.3.2 Visualization of velocity and stress fields

We consider a narrow channel ($L = 4D$) with no-slip walls. Figure 16 collects plots of the velocity and stress fields across the domain. The pressure field is of special interest as it features a few notable phenomenons:

- First, it validates the benefit of allowing the dilation of the flow, as the pressure in the wake of the obstacle is indeed zero;
- The zone of highest pressure is not located at the very front of the obstacle. Instead, we observe the formation of high-pressure arch above this point;
- Above this arch, there exists a region where the pressure is lower than further upstream; moreover the transition between this two zone is very abrupt, as shown by the absence of two isosurfaces on the figure. Note that this phenomenon disappears when considering free-slip boundary conditions for the channel walls.

6.4 Performance

We now study the computational performance for the problem of Section 4 – the dynamics case is just a succession of such problems.

In order to make as fair a comparison as possible, to evaluate the current error at each fixed-point iteration we chose not to use a residual based on a projection operator — which are known to be disavantadgeous for interior-points — but rather the **SOC** Fischer-Burmeister function for frictional problems as defined e.g. in [DBDB11].

We consider the silo geometry of section 6.2.3, a $\mathbb{P}_2 - \mathbb{P}_{1d}$ FEM approximation order, and a rheology with $\mu = 0.5$, Re = 1 and Bi = 0. The base mesh has a resolution of 640 vertices.

Figure 17 shows typical convergence plots for selected algorithms. Table 2 shows the evolution of the computation time in seconds as the mesh is refined, for an interior-point method and a Spectral Projected Gradient method. The latter, despite its simplicity, is therefore highly competitive.

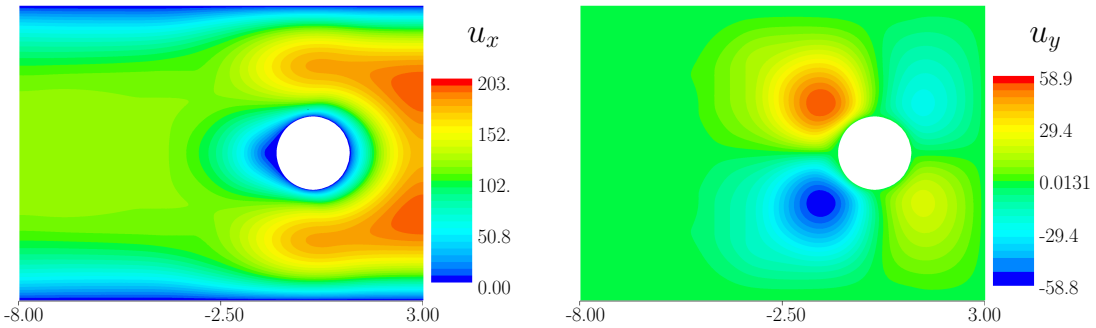

(a) Axial velocity u_x

(b) Perpendicular velocity u_y

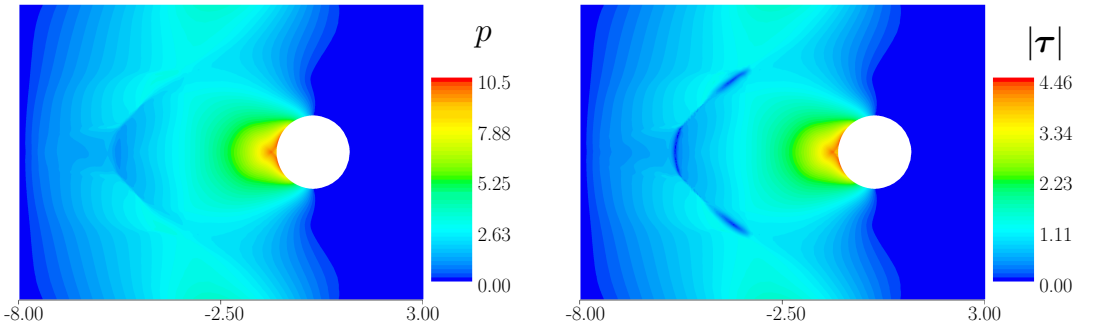

(c) Pressure p

(d) Norm of frictional stress $|\boldsymbol{\tau}|$

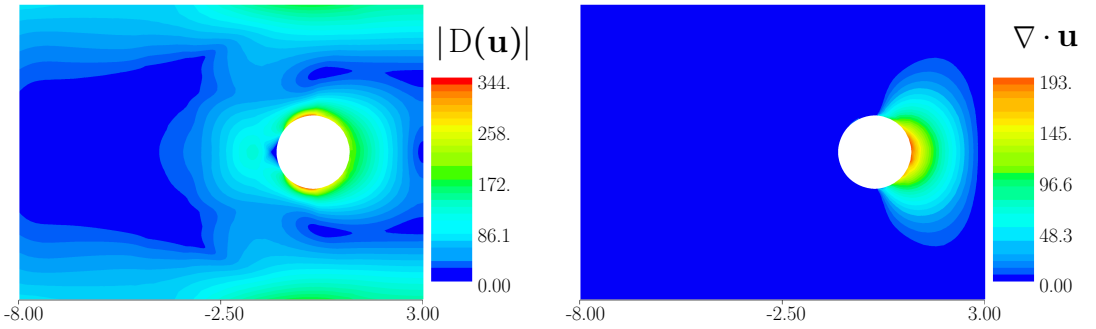

(e) Shear rate $|\mathrm{D}(\mathbf{u})|$

(f) Divergence of velocity $\nabla \cdot \mathbf{u}$

Figure 16: Velocity and stress fields for the flow around a cylinder in a narrow channel, with $\mu = 0.3$, $\mathrm{Re} = 100$, $\mathrm{Bi} = 0$ and $\tilde{D} = \frac{1}{4}$

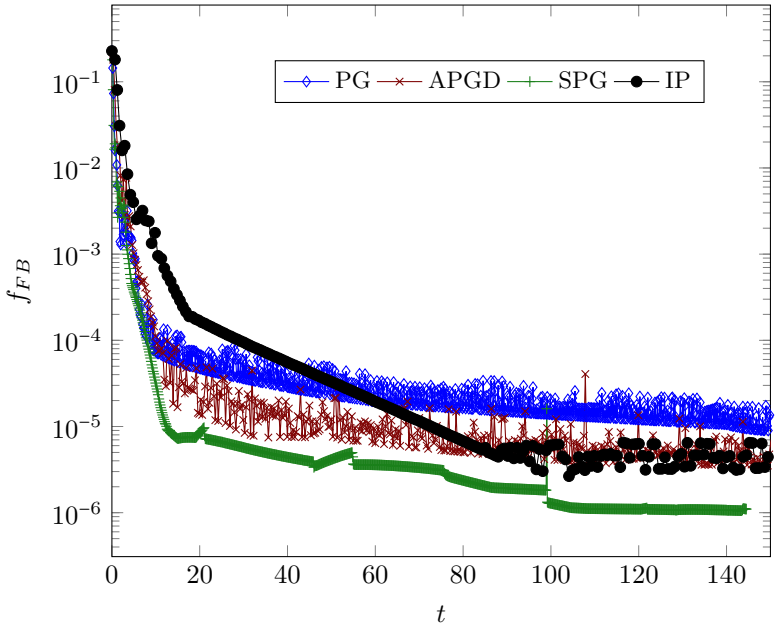

Figure 17: Infinity-norm of the Fischer-Burmeister function as a function of the wall time for the Projected-Gradient, Accelerated Projected Gradient Descent, Spectral Projected Gradient and Interior Points algorithm

	Mesh 1			Mesh 2			Mesh 3			Mesh 4		
	t	n	t/n	t	n	t/n	t	n	t/n	t	n	t/n
Mosek	71	100	0.71	116	29	4	564	23	24	6281	17	369
SPG	13	88	0.14	69	79	0.88	144	33	4.4	1098	47	23

Table 2: Comparison of time taken to reach a give tolerance for 4 meshes with respectively 670, 2703, 10403 and 41509 vertices. The columns headers t, n, and t/n give the total wall time in seconds, the number of iterations of the fixed-point algorithm and the average time per iteration.

7 Discussion

7.1 Limitations

The main limitation of our approach appears to be its computational cost. The **SOCP** formulation becomes quickly expensive when the number of required fixed-point iterations increases, while the Projected Gradient requires solving at least one linear system at each inner iteration. This makes three-dimensional scenarios only tractable for rough meshes. However, note that for the timestepping algorithm without Newtonian viscosity ($\mathrm{Re} = +\infty$), the inverse of the A matrix will be sparse for certain discretizations of $V(\Omega)$. The explicit computation of the Delassus operator would then become possible. This could speed up the proposed method, or allow for the use of other algorithms such as Gauss–Seidel based ones [JAJ98, DBDB11].

From a physics point of view, the fact that we do not take into account a variable density could lead to errors in zones where the local divergence is strictly positive, such as regions in the wake of obstacles. Our treatment of boundary conditions is also limited. We should consider more realistic laws, such as Coulombic ones. Moreover, some physical

factors describing granular matter are lacking to the model. The equations that we retrieve are analogous to those of inelastic contact mechanics, while a non-zero restitution coefficient might be necessary to properly model some classes of granular flows.

7.2 Conclusion and future work

In this work we have introduced a macroscopic, continuous model for granular-like flows, and we have shown that it was driven by equations structurally similar to those appearing in contact mechanics between discrete elements. We have then exibited algorithms for solving those equations on a class of spatial discretization and demonstrated that they were well-defined.

These new numerical simulation tools allowed us to capture the typical non-smooth effects critical to the simulation of yield-stress flows, as well as to accommodate complex rheologies such as the well-known $\mu(I)$ rheology. The main advantage over most previous approaches is the absence of any regularization or clamping. The formulation in the framework of Second Order Cone Programing paves the way for methods with superlinear convergence rates.

In future work we plan to extend our approach to dry flows with varying volumic fraction of grains. On the computational side, we would also like to devise more efficient solvers, in order to make three-dimensional scenarios tractable.

Acknowledgement

This work has been partially supported by the LabEx PERSYVAL-Lab (ANR-11-LABX-0025-01) funded by the French program Investissement d'avenir.

References

[AC91] P. Alart and A. Curnier. A mixed formulation for frictional contact problems prone to Newton like solution methods. *Computer Methods in Applied Mechanics and Engineering*, 92(3):353–375, nov 1991.

[ACLM11] V. Acary, F. Cadoux, C. Lemaréchal, and J. Malick. A formulation of the linear discrete coulomb friction problem via convex optimization. *ZAMM - Journal of Applied Mathematics and Mechanics / Zeitschrift für Angewandte Mathematik und Mechanik*, 91(2):155–175, 2011.

[AID12] P. Alart, D. Iceta, and D. Dureisseix. A nonlinear domain decomposition formulation with application to granular dynamics. *Computer Methods in Applied Mechanics and Engineering*, 205-208:59–67, jan 2012.

[ART03] E.D. Andersen, C. Roos, and T. Terlaky. On implementing a primal-dual interior-point method for conic quadratic optimization. *Mathematical Programming*, 95(2):249–277, feb 2003.

[BB88] Jonathan Barzilai and Jonathan M. Borwein. Two-point step size gradient methods. *IMA Journal of Numerical Analysis*, 8(1):141–148, 1988.

[BBS00] S.G. Bardenhagen, J.U. Brackbill, and D. Sulsky. The material-point method for granular materials. *Computer Methods in Applied Mechanics and Engineering*, 187(3-4):529–541, jul 2000.

[BLvdV61] W.A. Beverloo, H.A. Leniger, and J. van de Velde. The flow of granular solids through orifices. *Chemical Engineering Science*, 15(3-4):260–269, sep 1961.

[BMdBC15] Jeremy Bleyer, Mathilde Maillard, Patrick de Buhan, and Philippe Coussot. Efficient numerical computations of yield stress fluid flows using second-order cone programming. *Computer Methods in Applied Mechanics and Engineering*, 283:599–614, jan 2015.

[Cad09] Florent Cadoux. *Optimization and convex analysis for nonsmooth dynamics*. Theses, Université Joseph-Fourier - Grenoble I, nov 2009.

[CM14] Julien Chauchat and Marc Médale. A three-dimensional numerical model for dense granular flows based on the mu(i) rheology. *Journal of Computational Physics*, 256:696–712, jan 2014.

[CZW03] D. Chehata, R. Zenit, and C. R. Wassgren. Dense granular flow around an immersed cylinder. *Physics of Fluids*, 15(6):1622, 2003.

[DBDB11] Gilles Daviet, Florence Bertails-Descoubes, and Laurence Boissieux. A hybrid iterative solver for robustly capturing coulomb friction in hair dynamics. *ACM Transactions on Graphics – SIGGRAPH Asia 2011*, 2011.

[DSF98] G. De Saxcé and Z.-Q. Feng. The bipotential method: a constructive approach to design the complete contact law with friction and improved numerical algorithms. *Math. Comput. Modelling*, 28(4-8):225–245, 1998.

[FG82] M Fortin and R Glowinski. Méthodes de lagrangien augmenté. application à la résolution numérique de problèmes aux limites. *Collection Méthodes Mathématiques de l'Informatique. Dunod*, 1982.

[FN05] I.A. Frigaard and C. Nouar. On the usage of viscosity regularisation methods for visco-plastic fluid flow computation. *Journal of Non-Newtonian Fluid Mechanics*, 127(1):1–26, apr 2005.

[GDR04] GDR MiDi. On dense granular flows. *The European Physical Journal E*, 14(4):341–365, aug 2004.

[Hey13] Toby D Heyn. *On the modeling, simulation, and visualization of many-body dynamics problems with friction and contact*. PhD thesis, THE UNIVERSITY OF WISCONSIN-MADISON, 2013.

[HT83] Jaroslav Haslinger and Miroslav Tvrdỳ. Approximation and numerical solution of contact problems with friction. *Aplikace matematiky*, 28(1):55–71, 1983.

[HUL01] J.-B. Hiriart-Urruty and C. Lemaréchal. *Fundamentals of convex analysis*. Grundlehren text editions. Springer, Berlin, New York, 2001.

[IMBR15] Ioan R. Ionescu, Anne Mangeney, François Bouchut, and Olivier Roche. Viscoplastic modeling of granular column collapse with pressure-dependent rheology. *Journal of Non-Newtonian Fluid Mechanics*, mar 2015.

[JAJ98] F. Jourdan, P. Alart, and M. Jean. A Gauss-Seidel like algorithm to solve frictional contact problems. *Computer Methods in Applied Mechanics and Engineering*, 155:31–47, 1998.

[Jea99] M. Jean. The non-smooth contact dynamics method. *Computer Methods in Applied Mechanics and Engineering*, 177(3-4):235–257, jul 1999.

[JFP06] Pierre Jop, Yoël Forterre, and Olivier Pouliquen. A constitutive law for dense granular flows. *Nature*, 441(7094):727–730, jun 2006.

[KSO14] Jan Kleinert, Bernd Simeon, and Martin Obermayr. An inexact interior point method for the large-scale simulation of granular material. *Computer Methods in Applied Mechanics and Engineering*, 278:567–598, aug 2014.

[LKA14] Keng-Wit Lim, Kristian Krabbenhoft, and José E. Andrade. A contact dynamics approach to the granular element method. *Computer Methods in Applied Mechanics and Engineering*, 268:557–573, jan 2014.

[LSP11] P.-Y. Lagrée, L. Staron, and S. Popinet. The granular column collapse as a continuum: validity of a two-dimensional navier–stokes model with a $\mu(i)$-rheology. *Journal of Fluid Mechanics*, 686:378–408, sep 2011.

[LZ99] Zhi-Quan Luo and Shuzhong Zhang. On extensions of the frank-wolfe theorems. *Computational Optimization and Applications*, 13(1/3):87–110, 1999.

[MJA+07] C. Mankoc, A. Janda, R. Arévalo, J. M. Pastor, I. Zuriguel, A. Garcimartín, and D. Maza. The flow rate of granular materials through an orifice. *Granular Matter*, 9(6):407–414, sep 2007.

[Mor99] J.J. Moreau. Numerical aspects of the sweeping process. *Computer Methods in Applied Mechanics and Engineering*, 177(3–4):329 – 349, 1999.

[Nes83] Yurii Nesterov. A method of solving a convex programming problem with convergence rate o (1/k2). *Soviet Mathematics Doklady*, 27(2):372–376, 1983.

[RA05] Mathieu Renouf and Pierre Alart. Conjugate gradient type algorithms for frictional multi-contact problems: applications to granular materials. *Computer Methods in Applied Mechanics and Engineering*, 194(18-20):2019–2041, may 2005.

[Sar12] Pierre Saramito. Efficient C++ finite element computing with Rheolef. oct 2012.

[Sar15] Pierre Saramito. Efficient C++ finite element computing with Rheolef. Lecture, sep 2015.

[SLP12] L. Staron, P.-Y. Lagrée, and S. Popinet. The granular silo as a continuum plastic flow: The hour-glass vs the clepsydra. *Physics of Fluids*, 24(10):103301, 2012.

[SLP14] L. Staron, P. Y. Lagrée, and S. Popinet. Continuum simulation of the discharge of the granular silo. *The European Physical Journal E*, 37(1), jan 2014.

[SR01] Pierre Saramito and Nicolas Roquet. An adaptive finite element method for viscoplastic fluid flows in pipes. *Computer Methods in Applied Mechanics and Engineering*, 190(40-41):5391–5412, jul 2001.

[Tas13] Alessandro Tasora. Efficient simulation of contacts, friction and constraints using a modified spectral projected gradient method. 2013.

[WW12] Christian Wellmann and Peter Wriggers. A two-scale model of granular materials. *Computer Methods in Applied Mechanics and Engineering*, 205-208:46–58, jan 2012.